AN ENHANCED METHOD FOR FULL-INVERSION-BASED ULTRASOUND ELASTOGRAPHY OF THE LIVER

MOHAMED ABOUTALEB

A THESIS SUBMITTED TO THE FACULTY OF GRADUATE STUDIES IN PARTIAL FULFILLMENT OF THE REQUIREMENTS FOR THE DEGREE OF MASTER OF APPLIED SCIENCE

GRADUATE PROGRAM IN
ELECTRICAL AND COMPUTER ENGINEERING
YORK UNIVERSITY
TORONTO, ONTARIO

August 2022

Abstract

Similar to many other types of cancer, liver cancer is associated with biological changes that lead to tissue stiffening. An effective imaging technique that can be used for liver cancer detection through visualizing tissue stiffness is ultrasound elastography. In this thesis, we show the effectiveness of an enhanced method of tissue motion tracking used in quasi-static ultrasound elastography for liver cancer assessment compared to other state of the art methods. The method utilizes initial estimates of axial and lateral displacement fields obtained using conventional time delay estimation (TDE) methods in conjunction with a recently proposed strain refinement algorithm to generate enhanced versions of the axial and lateral strain images. Another primary objective of this work is to investigate the sensitivity of the proposed method to the quality of these initial displacement estimates. The proposed algorithm is founded on the tissue mechanics principles of incompressibility and strain compatibility. Tissue strain images can serve as input for full-inversion-based elasticity image reconstruction algorithm. In this work, we applied strain images generated by the proposed method in conjunction with an iterative elasticity reconstruction algorithm for full-inversion-based liver elastography. Moreover, a set of *in-silico* experiments were conducted to validate the assumptions used in the reconstruction technique to improve the realism of the method. Ultrasound RF data collected from a tissue-mimicking phantom and from four liver cancer patients who underwent open surgical RF thermal ablation therapy were used to evaluate the proposed method. The results showed that the proposed method produces superior results to other state of the art methods. Moreover, while there is some sensitivity to the displacement field initial estimates, overall, the proposed method is robust to the quality of the initial estimates.

Acknowledgments

I wish to express my sincere gratitude to my supervisors Dr. Ali Sadeghi-Naini and Dr. Abbas Samani for their continuous support and guidance throughout this research. Special thanks to Dr. Tabatabaei for serving on my supervisory committee. Moreover, I also wish to thank my lab mates Niusha Kheirkhah, Seyed Ali Jalalifar, Reza Yaghoubi, and Shirin Saednia for their help.

I would like to thank my family and friends and dedicate this thesis to them, for their continuous love, support, and encouragement.

Table of Content

List of Tables

List of Figures

Chapter 1

Introduction

1.1 Cancer

One of the leading causes of global mortality and morbidity is cancer [1]. During cancer development, that may start in different organs and tissues, the cells grow uncontrollably and possibly spread to other parts in the body. As a natural process, cells regenerate to replace older and damaged ones. However, this process can break down as a result of faulty DNA replication, leading cells with faulty DNA to multiply out of control before a cancerous tumor is formed. Cancerous tumors, also known as malignant tumors, differ from benign masses as they can spread into nearby tissue or even farther parts in the body, forming other tumors in a process called metastasis. In contrast, benign masses do not spread into other body sites, and unlike cancerous tumors, they can be surgically removed safely without the need for adjuvant therapy [2].

1.2 Liver Anatomy

Liver is the second largest organ in the human body, weighting about 3 pounds. Protected by the rib cage, the liver sits on the right side of the abdomen. As illustrated in Figure 1-1, it mainly consists of two large sections of the right and left lobes. The cells that make up the liver parenchyma are called hepatocytes. These cells are present in the liver in conjunction with other types of cells that line its blood vessels and bile ducts [3]. Part of the pancreas and intensities are situated under the liver, along with the gallbladder. The liver's main function is to filter the blood which leaves the stomach and intestines before it is passed through to the rest of the body. It also provides several other functions, such as metabolizing drugs into forms that are accepted more easily by the rest of the body, producing certain proteins for the blood plasma, and regulating blood

clotting [4]. The liver parenchyma exhibits viscoelastic properties while it is incompressible, meaning that it undergoes deformation without changing its volume. The viscoelastic behavior is attributed to high vascularity in the liver tissue and the complex extracellular matrix (ECM). The liver ECM is a heterogenous soft scaffold composed of proteins such as collagen. The composition and microstructure of ECM and its interaction with stromal cells play a major role in regulating the tissue stiffness [5]. The ECM of liver tumors, which is primarily composed of fibrous tissue, becomes stiffer due to an increase of fiber cross-linking. Therefore, tissue stiffness can be used as a contrast mechanism for imaging the liver of liver cancer patients.

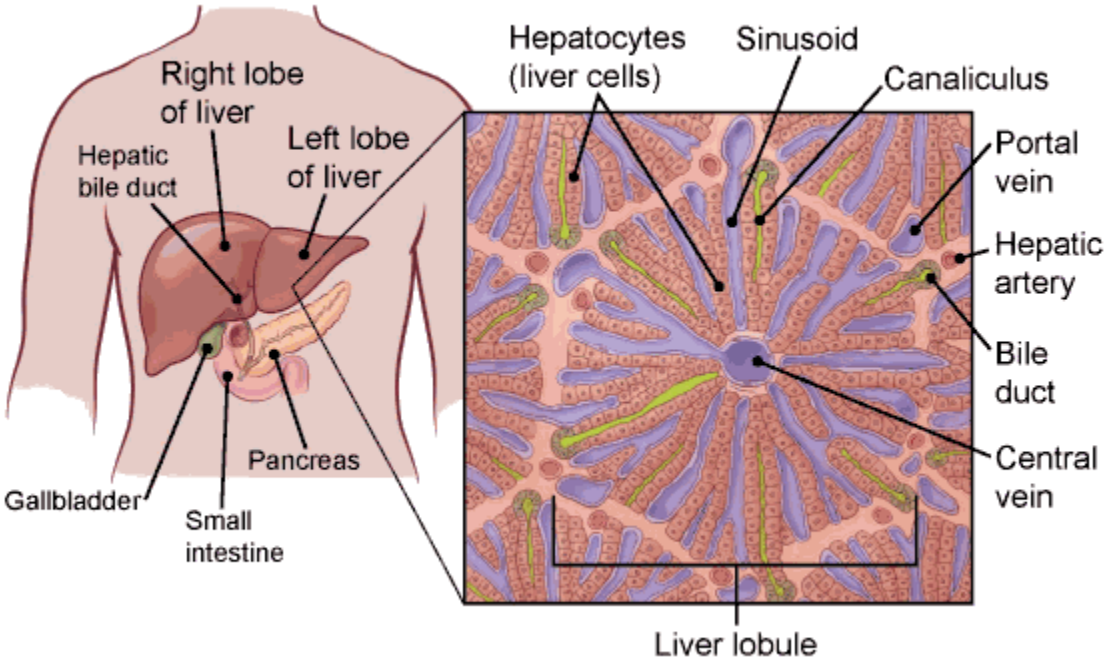

Figure 1-1 Liver anatomy [6].

1.3 Liver Cancer

Liver cancer is the sixth most commonly occurring cancer in the world, with its incidence being tripled since 1980 [7]. In the United States, it is expected that 41,260 adults will be diagnosed with liver cancer in 2022. In the same year, it is estimated that this disease will lead to 30,520 deaths in the United States [8], while it is the third leading cause of cancer death worldwide [7].

Primary liver cancer is a malignancy that starts in the liver. Different types of primary liver cancer include hepatocellular carcinoma (HCC), intrahepatic cholangiocarcinoma or bile duct cancer, angiosarcoma and hepatoblastoma [3]. HCC is the most common form of liver cancer in adults. Its growth pattern can be from a single tumor that grows larger, or starting as many small cancer nodules throughout the liver. The second is mostly found in cases with cirrhosis (chronic liver damage). In some part of the world however, secondary (metastatic) liver cancer is more common than primary liver cancer. Liver nodules that are benign also occur, types of it are hemangioma, hepatic adenoma, and focal nodular hyperplasia [3]. However, the most occurring type of liver cancer does not originate from the liver but is spread from neighboring organs such as the pancreas, stomach, or colon [3]. This type of cancer is called secondary liver cancer or liver metastasis.

Several factors can increase the risk of liver cancer. Chronic infection with hepatitis B virus or hepatitis C virus are responsible for most cases of primary liver cancer, as these infections lead to liver cirrhosis[9]. Other risk factors include nonalcoholic liver disease, diabetes, and excessive alcohol consumption. Symptoms of liver cancer do not appear in the early stages in most patients. The symptoms that appear in later stages can include loss of appetite, weight loss, fatigue, and yellow discoloration of the eyes and the skin [9].

Associated with liver cancer is liver tissue stiffening due to collagen deposition and microstructural changes. As such, increased tissue stiffness is an indicator of many solid tumors [10]. Interaction of extracellular matrix (ECM) and stromal cells play a role in regulating the tissue stiffness [5]. The ECM of tumors, primarily composed of fibrous tissue, becomes stiffer due to an increase of fiber cross-linking.

1.4 Liver Cancer Detection and Diagnosis

Evidence shows that it is crucial to detect liver cancer early to devise effective treatment, hence increasing the chances of survival [3]. The gold standard approach for liver cancer diagnosis is biopsy. However, it is an invasive method with a risk of mortality of 3 in 10,000 [11]. Furthermore, because only 1/50,000 of the liver volume is typically sampled through biopsy, it is prone to sampling errors. Imaging modalities that are commonly used for detection and characterization of focal liver lesions include contrast enhanced ultrasonography (US), computed tomography (CT), magnetic resonance imaging (MRI), positron emission tomography (PET). These modalities have their own advantages and limitations that makes it suitable for specific applications. In this section, each of these methods are described.

1.4.1 Computed Tomography (CT)

Computed tomography (CT) imaging is a non-invasive imaging modality that uses a combination of X-ray data acquisition at different angles and computer technology to reconstruct 3D images of the body. In protectional X-ray radiography, an X-ray machine emits a burst of X-rays that pass through the body then received by a negative film or digital detector on the other side of the body, leading to an image formation. As such, the depth information is lost in the generated 2D projectional images and many details about internal organs cannot be captured on them. In CT

imaging, the X-ray source revolves around the body, which allows acquiring different projections of the same organ. The acquired projections are processed on a computer to reconstruct 3D volumetric images that can show different cross-sections of the body. In some cases, with lesions greater than 1 cm, triple-phase, contrast enhanced CT is used for liver imaging [12]. The contrast agent is often an iodine-based chemical substance taken orally or injected into the body that results in higher imaging contrast for the liver, as the structures such as blood vessels are highlighted. Contrast enhanced CT has high sensitivity and specificity in detecting hepatic metastases [13]. Another benefit is the availability of CT compared to other modalities such as PET and MRI which provides easier access. However, if the patient suffers from iodine allergy which restricts the use of the radiographic contrast agent, then CT would produce low accuracy results. Another limitation is the radiation exposure on the patient.

1.4.2 Magnetic Resonance Imaging (MRI)

In MRI, the scanner produces a strong static magnetic field that causes the hydrogen protons in the body to align with the field. The protons are stimulated by radiofrequency magnetic field that is emitted through the patient, causing the protons to spin out of the equilibrium state and resisting the pull of the magnetic field. Consequently, when the radiofrequency pulse is turned off, the receiver coils detect the energy released as the protons realign with the static magnetic field. The amount of energy released and the time it takes for the protons to realign with the magnetic field are affected by the tissue environment and its chemical characterization [14] These magnetic properties can help physicians distinguish between different types of tissues, including healthy and pathological tissues. Contrast agents may also be given to the patient intravenously. Contrast agent-enhanced MRI has shown superior results over contrast-enhanced CT and non-contrast MRI [13]. Nevertheless, MRI has limitations with patients who have metallic materials within their

body (artificial joints, heart pacemakers, artificial heart valves, etc.) cannot be scanned with MRI. Furthermore, the use of contrast agents can have side effects on certain patients as [15]. Moreover, due to the high cost of MRI machines, their availability is limited.

1.4.3 Positron Emission Tomography (PET)

Positron emission tomography is a nuclear medicine imaging modality. It applies radioactive contrast agents made up of a radioactive isotope that is attached to a material used in the body, usually sugar. Such contrast agents are further absorbed by cells that use a lot of energy, such as cancer cells, as they travel through the body. A precise ring of detectors around the subject records pairs of antiparallel gamma rays produced as result of positron annihilation. Positrons are the positively charged particles released by the radioactive material after a beta-plus decay. The gamma ray recordings are processed on a computer to generate 3D images of radioactivity inside the body [16]. For the liver, a PET-CT examination is a preferred approach as it allows for anatomic localization of 'hot-spots' for characterization, as well as higher sensitivity for detecting hepatic metastases. Given the higher cost of PET and subsequently its limited availability, PET is not used in routine examinations.

1.4.4 Ultrasound (US) Imaging

Conventional ultrasound imaging produces B-mode (brightness-mode) image, where a transducer emits ultrasound pulses and detects the echoes generated by acoustic scatterers within the ultrasound beam. As ultrasound waves travel through tissue with different acoustic properties, partial energy of ultrasound pulses is reflected back to the probe in the form of ultrasound echoes. Using the speed of sound, and the magnitude and arrival time of the echo, a computer can generate structural images of the underlying tissues as 2-dimensional images, known as B-mode image. The

brightness of each pixel is translated from the strength of the corresponding echo received. Using sound waves instead of ionizing radiation and while normally not requiring injection of contrast agents, makes US a safe imaging alternative. Ultrasonography has been used in medical imaging for over 50 years, mainly for its simplicity of operation, real-time capability, portability, and low cost [17]. Conventional ultrasonography generates anatomical images of organs. However, it does not provide information on tissue biomechanical properties. Several diseases and abnormalities including cancer cause alterations in tissue stiffness [17]. Therefore, tissue stiffness can be used as contrast mechanism for imaging to detect and characterize such abnormalities. Ultrasound elastography (USE) techniques have been emerged on the basis of using tissue elasticity as the mechanism of contrast to image different tissue types.

1.4.5 Ultrasound Elastography (USE)

Elastography imaging includes a class of imaging techniques that use tissue stiffness as a contrast mechanism. Ultrasound elastography is among the first proposed methods of elasticity imaging, which can provide clinically relevant information and can be used for tissue characterization of deeper organs. This technique involves mechanical stimulation to deform the tissue or generate wave in it before the data pertaining to deformation or wave pattern can be used to create images of the tissue stiffness. Depending on the mechanical stimuli, elastography techniques can be classified into quasi-static or dynamic (harmonic) elastography. In quasi-static methods, tissue stiffness maps are estimated from the analysis of the tissue strain generated by the quasi-static mechanical stimulation. Dynamic elastography is performed by imaging of shear waves, generated by dynamic stimulation, whose propagation is governed by the tissue stiffness distribution. The main stiffness parameters that linear elastography techniques aim to quantitatively image are the Young's modulus (E) or shear modulus (G). The Young's modulus demonstrates meaningful

variations among different biological tissues, making it suitable for tissue characterization. USE techniques permit quantitative assessment of liver stiffness; they also have the potential to monitor these histopathologic changes to aid with liver treatment methods. According to [18], while healthy liver tissue has a Young's modulus value of 640 pascals under 5% preload strain, a liver tumor sample tested under the same preload strain exhibits a Young's modulus of 3000 pascals. Hence, the Young's modulus can be regarded as a quantitative reproduction of a clinician's palpation capable of providing relevant quantitative diagnostic information.

1.4.6 Liver Imaging Reporting and Data System

The Liver Imaging Reporting and Data System (LI-RADS) standardizes the reporting of imaging for HCC in the process of screening, diagnosis and treatment response assessment [19]. There are four categorizes of LI-RADS for different clinical contexts including the US LI-RADS for surveillance, the CT/MRI LI-RADS for diagnosis, the contrast enhanced US LI-RADS for diagnosis, and CT/MRI LI-RADS for treatment response assessment. An example of the reporting system for US LI-RADS is shown in Table 1-1.

Table 1-1. US LI-RADS scores [19].

US Categories	Definition
US-1: Negative	No observation/Only definitely benign observation
US-2: Subthreshold	Observations < 10 mm in diameter, not definitely benign
US-3: Positive	Observations ≥ 10 mm in diameter, not definitely benign Or Observation might be a solid nodule of any echogenicity or are of parenchymal distortion ≥ 10mm

1.5 Liver Cancer Treatment

Liver cancer treatment is most effective when planned according to the cancer stage of the patient. Treatment strategies selection is complex due to multiple factors such as underlying liver function, size and location of the tumor and the condition of the patient. Studies report that the highest survival rates are achieved when the hepatocellular carcinoma (HCC) can be removed surgically, or by liver transplantation [12]. Between localized, metastatic, and recurrent stage HCC, several treatment options are suggested. For localized and recurrent HCC, standard treatment methods include surgical resection, liver transplantation, and ablation therapy. The core treatment of HCC is the surgical resection, where only 5% to 10% of patients, who meet certain criteria for resection, can be considered [12]. Liver transplantation is a possible curative solution for HCC, where patients with lesions smaller than 3 cm are eligible for. However, the scarcity of the liver donors restricts the availability of this treatment. Chemotherapy is the most common treatment for liver metastases, which is also used sometimes to shrink the tumor ahead of resection surgery. Targeted therapy and ablation are also considered for metastases treatment. Ablation therapy is done through minimally invasive or open surgery when tumor excision is not feasible. Tumor ablation is performed by changing the temperature of tissue, which is usually done by radiofrequency ablation (RFA), exposure to chemical substance, and by direct damage to the cell membrane. While RFA can cause complications, the rate of complication is lower than the excision techniques. Invasive treatments require an accurate lesion localization for a precise and safe treatment.

1.5.1 Intra-operative Imaging

Acquiring information about the liver tumor such as its size and location during surgery is a necessity. Liver palpation is one of the options used to provide information during surgeries, but it is limited to large palpable tumors, while it is a subjective method and its accuracy depends on

the experience of the surgeon. One of the main imaging methods that can be used effectively to evaluate the tumors during surgery is intra-operative ultrasonography (IOUS). However, small, and iso-echoic tumors within pathological livers are sometimes difficult to detect. Therefore, information about tissue stiffness can aid in more accurate identification of position and size of the tumors [20]. Results obtained in this research show that real-time tissue elastography can enable intraoperative imaging to distinguish between the two most common malignancies, HCC, and metastatic adenocarcinoma relatively accurately.

Successful ablation can be achieved when there is enough information about the targeted tissue. The RFA and other ablation procedures are conducted by timing the exposure of the tissue to radiation or the chemical agent, which affects the magnitude of tissue damage. Features of liver anatomy such as blood vessels, connective tissue, and gas influences the rate of tissue damage when ablation is applied along the radius of target area. Research has been conducted to assess microwave ablation on liver tissue through using MR elastography combined with conventional MRI. Previous literature [21] has found that MRE was just as effective in finding baseline tumor stiffness to obtain the optimal ablation energy required to break it down. The use of RFA probe to induce displacement in liver tissue in conjunction with ultrasound data acquisition to acquire images of elastic modulus of thermal lesions was investigated in [22]. Their results from *in-vivo* experiments show the feasibility of obtaining accurate stiffness properties of thermal lesions, demonstrating the feasibility of *in-vivo* imaging in deep tissues, which can aid in assessing the outcome of tumor ablation procedure. The US-based systems are routinely used to monitor liver tumor ablation, hence the higher feasibility of USE compared to MRE. This can also eliminate the need for US contrast agent, which is one of the techniques used for tissue ablation monitoring.

1.6 Elastography

1.6.1 Quasi-Static Strain Imaging

In ultrasound elastography (USE), quasi-static strain imaging was the first technique introduced in 1991 [23]. In this technique, displacement fields resulting from quasi-static mechanical stimulation of tissue, that is often applied by the probe, are calculated before strain images are generated [17]. Ultrasound radiofrequency data is acquired at pre- and post- compression states before the tissue displacement in axial and lateral directions can be estimated. Figure 1-2 illustrates a schematic tissue mimicking phantom under the two states of before and after compression generated by the US probe. Using spatial differentiation of the estimated displacement fields, the axial and lateral strain images can be produced. Strain images can be used directly as an approximation to the tissue stiffness distribution. While often capable of detecting abnormalities, strain imaging does not provide reliable estimates of the stiffness as it is founded on stress uniformity assumption. To account for the tissue stress non-uniformity, full-inversion-based elastic modulus reconstruction techniques have been developed [24].

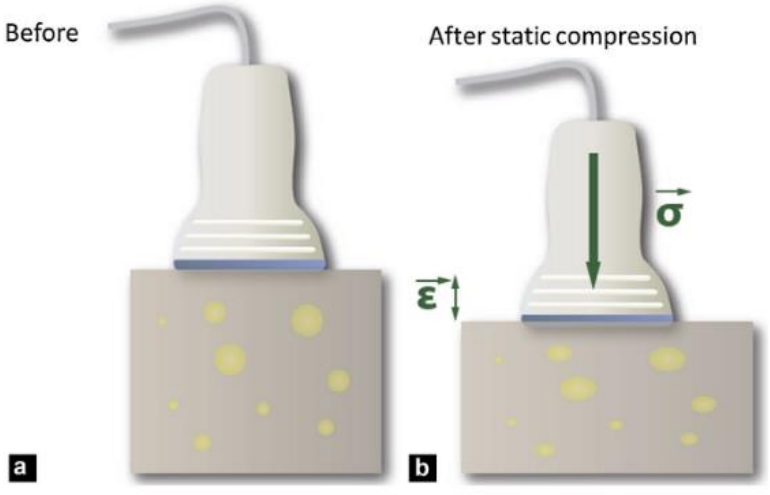

Figure 1-2. Quasi static compression using an ultrasound probe. The state of a schematic heterogenous phantom is shown before (a) and after (b) static compression. Σ and ε denote the applied stress and generated strain, respectively [17].

1.6.2 Quasi-Static Elastic Modulus Imaging

In these techniques, the distribution of ratio of Young's modulus of tumor to background (healthy) tissue is reconstructed by solving the elasticity equations within an inverse problem framework, using the displacement fields estimated via quasi-static USE. While tissue Young's modulus can be advantageous in certain applications, the ratio which shows tissue stiffening is highly advantageous as it automatically factors in tissue stiffness inter-variability of patients. It is noteworthy that reconstruction of the distribution of the absolute Young's modulus requires acquisition of force information of tissue mechanical stimulation which is not performed in conventional USE techniques. In the context of image reconstruction, Young's modulus (elastic modulus) and Young's modulus (elastic modulus) ratio have been used interchangeably to refer to the Young's modulus ratio throughout the thesis. The elastic modulus ratio reconstruction problem can be formulated using linear inversion, nonlinear optimization or iterative procedures. In the latter, the tissue Young's modulus distribution is reconstructed iteratively by computing stress distribution using finite element method (FEM) followed by Young's modulus estimation using Hooke's law.

Previous works on liver tissue stiffness assessment using quasi-static elastography include [25] and [26] where the goal was estimating the strain field using acquired ultrasound RF data to approximate stiffness. To the best of our knowledge, no previous work has been carried out for full-inversion-based elastic modulus reconstruction in the liver.

Despite being ill-posed, elasticity reconstruction techniques use axial displacement field only for Young's modulus (E) reconstruction as the quality of lateral displacement fields obtained from US based motion tracking techniques is low. The ill-posedness can be mitigated by enriching the input

displacement data and enhancing its quality. To that end, several research groups have developed methods to achieve this goal. Some of these methods have been described in Chapter 2.

1.6.3 Dynamic Elastography

In dynamic or shear wave ultrasound elastography methods, pushing acoustic pulses or mechanical vibration actuators are employed for mechanical stimulation that leads to generation and propagation of shear wave in the tissue [17]. Shear waves are generated at low frequencies (10 Hz to 2000 Hz), as higher frequencies are associated with high energy dissipation and limiting wave penetration [17]. The generated wave propagates slowly where the speed (V_s: 1-50 m/s) is directly related to the medium shear modulus $\mu = \rho V_s^2$. In this equation, ρ is the density of the medium which mostly consists of water (1000 kg/m^3). Progression of shear waves is monitored by ultrasound imaging; their velocity is estimated using the images acquired over the mechanical stimulation course. Dynamic elastography techniques, which rely on shear wave propagation, can produce quantitative and higher resolution Young's modulus map compared to quasi-static methods. Shear wave generation and data acquisition, however, requires a more complicated system. A number of shear-wave imaging methods implemented on different scanners have been shown in Figure 1-3. These methods include 1D transient elastography (1D-TE) that utilizes a mechanical vibrating device, as well as the point shear-wave elastography (pSWE) and 2D shear wave elastography (2D-SWE) that applies acoustic radiation forces for dynamic stimulation of tissue.

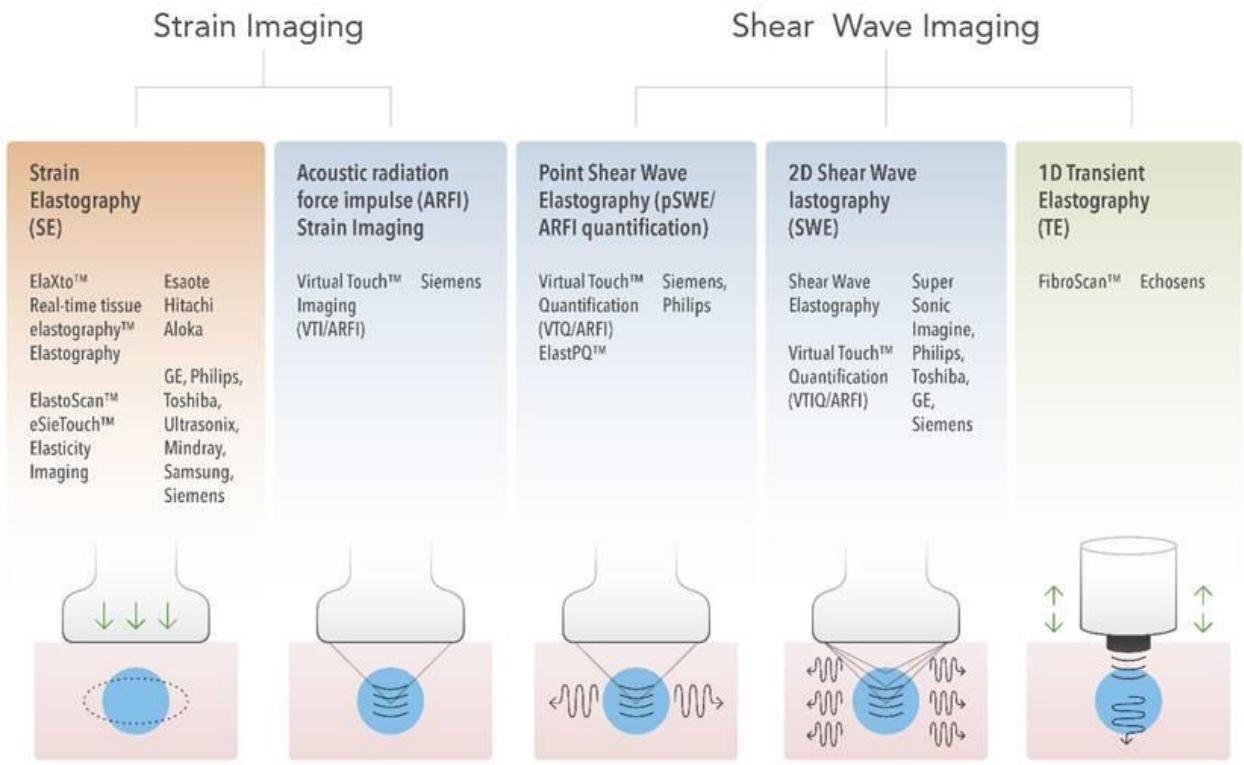

Figure 1-3. Ultrasound Elastography techniques [27].

1.7 Research objectives

The overarching goal of this thesis project is to develop and investigate an enhanced ultrasound elastography technique to characterize liver cancer in applications where external mechanical stimulation is possible. This includes thermal ablation of liver tumors where accurate tumor outline detection is paramount for successful therapy. The main objectives of the project include: (1) to adapt an enhanced ultrasound strain imaging method for the liver assessment, which was developed based on tissue mechanics principles of incompressibility and strain compatibility. (2) To develop a 3D finite element model of the liver and investigate/compare the accuracy of plane strain and plane stress models for the liver 2D finite element analyses. The outcome of this investigation is used in a full-inversion-based elastic modulus reconstruction technique of Objective 3. (3) To adapt a quasi-static full-inversion based elastic modulus reconstruction

technique for liver elastography using the enhanced strain images and iterative 2D finite element analysis with proper assumption and parameters, and (4) to evaluate and compare the performance of the developed techniques in strain imaging and elastic modulus reconstruction with different displacement initial guesses ranging from high quality ones obtained from the state-of-the-art methods to low quality ones obtained from less-advanced TDE-based strain imaging methods.

Chapter 2

Background and Literature Review

2.1 Elastography in Clinical Studies on the Liver

As USE techniques permit quantitative assessment of liver stiffness, their clinical use has been investigated to characterize liver lesions. Strain elastography and shear-wave elastography can be used to evaluate focal liver lesions. Acoustic radiation force impulse (ARFI) strain imaging has been used to estimate stiffness of the liver masses. This method, however, fails to distinguish between benign and malignant tumors, as they lack necessary accuracy for stiffness quantification of liver tissue abnormalities [28]. The pSWE has several advantages over older shear wave imaging methods, as the operator is able to choose a uniform area of the liver parenchyma before directly visualizing it using B-mode US. It is also less sensitive to ascites and obesity as the shear waves are generated locally inside the liver. Studies that investigated the accuracy of pSWE clinically in differentiating benign and malignant liver lesions have reported diagnostic accuracy of over 80% [29] [30]. Elastography in liver application face some limitations, as it is preferable to measure stiffness in the right lobe of the liver over the left lobe. This preference is due to internal mechanical simulations generated by the heart contractions that cause substantial interference with the externally generated waves in the left lobe. Moreover, methods that cause excitation at the skin surface are limited by patient obesity [27]. Transient USE, which is implemented in Fibroscan [31] utilizes a single element transducer used as emitter and receiver, for creating a small length transient vibration. Despite its advantages of being portable and inexpensive, it fails to localize and measure the stiffness in hepatic tissues and to evaluate fibrosis in the presence of liver lesions [32].

Magnetic Resonance Elastography (MRE) has also been applied to the liver and has shown high sensitivity and accuracy compared to US [33]. However, US and USE, which are readily available and inexpensive unlike MRE, can be potentially used widely for diagnosing and staging of liver cancer and fibrosis.

2.2 Displacement estimation for US Strain Imaging

Ultrasound strain elastography techniques vary in the way they generate tissue deformation. Methods to induce tissue deformation in strain imaging can be classified into direct mechanical excitation and acoustic radiation force excitation [27]. To generate axial and lateral displacement fields, ultrasound radiofrequency (RF) data is acquired at pre- and post-compression states before corresponding strain images are produced by differentiating the displacement fields. Time delay estimation (TDE) method, also known as speckle tracking, uses the RF data acquired to produce the displacement field [35]. Having infinitesimal tissue deformations, corresponding strain images are then generated by differentiating the displacement fields spatially using Equation (2-1).

$$\epsilon_x = \frac{\partial u_x}{\partial x} \tag{2-1}$$

Where ϵ_x is the axial strain and u_x is the axial displacement. Similarly, the lateral strains are calculated by differentiating the lateral displacements. It is noteworthy that the strain induced in the liver tissue in quasi-static elastography pertains to the strain induced in the tissue relative to the precompression state. This strain is sufficiently small to be considered infinitesimal. There are different techniques that implement TDE. The most common are window-based techniques as presented in [34], [35], where each window contains segments of the RF data. Methods such as normalized cross correlation (NCC) [36] or zero-phase crossing [37] are used to estimate the time delay of each window. The resolution of displacement field produced by this technique depends

on the window size chosen, and the occurrence of overlap between adjacent windows. A larger window size sacrifices the resolution but produces a smoother displacement map, whereas a smaller window produces a higher resolution, while leading to increased amount of noise in the estimated field. This can be improved, however, by filtering the output displacement map.

Displacement estimation can be considered as an optical flow problem with two B-mode images corresponding to the tissue pre- and post-compression states as the input [38]. Machine learning based TDE methods based on optical flow have also been proposed and have shown promising results [39]. However, they still require further development, and they require extensive training to achieve the task of speckle tracking.

Another technique of achieving TDE is regularized optimization, as in [26], [40]. In this approach, the time delay is estimated by optimizing a penalty function consisting of a regularization term. Methods founded on this approach assume displacement continuity which is necessary as it aligns with the tissue deformation physics. Tissue mechanics-based methods that incorporate tissue incompressibility and other tissue mechanics constraints have also been developed and have shown enhanced axial and lateral displacement maps [41], [42]. A number of TDE-based methods that have been used in this thesis project are described in more details in the next two subsections.

2.2.1 Time Delay Estimation Methods

The TDE methods include the dynamic programming and 2D analytic minimization (AM2D) algorithm proposed in [25]. In this method, the displacement field is initially estimated using dynamic programming (DP). This is a pixel precision method which is performed using a single seed line in the RF ultrasound frame and two successive sample spacing, which is then refined to a subpixel precision using analytic minimization (AM). A recently developed technique referred

to as the global ultrasound elastography (GLUE) calculates axial and lateral displacements through dynamic programming before their refinement through optimizing a non-linear cost function consisting of data amplitude similarity and spatial continuity terms [26]. This method differs from previous TDE methods by using a cost function that is formulated for the entire image instead of a single RF-line. Figure 2-1 illustrates the differences between GLUE and previous methods. To solve the cost function in GLUE, they use Taylor expansion similar to the approach described in [25] to arrive at a linear system of equations. The main steps of the GLUE technique for ultrasound strain imaging are given below:

1. Estimation of integer (number of pixels) displacements using dynamic programming (DP).
2. Refinement of the displacement field estimates using 2D optimization.
3. Generating strain images by spatially differentiating the displacement field.

A more recent method, second order ultrasound elastography (SOUL) [40], was recently developed. Similar to GLUE, it involves obtaining an initial displacement estimate using DP, however, unlike GLUE which is refined based on a 1^{st} order derivative smoothing term, it is refined by optimizing a penalty function containing echo similarity and a Laplacian regularization term. The first-order continuity constraint used in GLUE is thought to be less effective in representing the mechanics of tissue deformation and therefore leads to a suboptimal noise suppression. Results show that the SOUL method, which incorporates a second-order regularization term in the cost function, produces a smoother strain image while maintaining the contrast between different mediums [40].

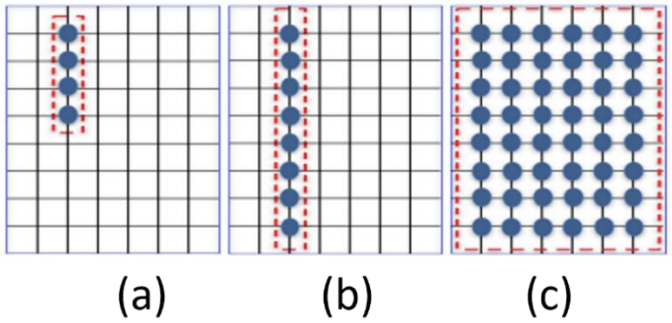

Figure 2-1. Comparison between the window-based methods for TDE. Circles represent RF samples that are used in TDE: (a) NCC: Few samples in an RF line are grouped together in a window for displacement calculation, (b) AM2D: Displacement is calculated using all samples in each RF line, and (c) GLUE: Entire RF frame is used for displacement calculation [26].

2.2.2 Tissue Mechanics-based Methods

Previous methods for displacement estimation do not utilize tissue mechanics constraints such as incompressibility and compatibility. Recent methods incorporated such constraints to obtain an improved displacement estimation. An algorithm using three US RF frames [43] incorporates these tissue mechanics principles, which are used to derive constraints on variations of the displacement field with time. These constraints are then used to generate a regularized cost function that incorporates amplitude similarity of three ultrasound images and displacement continuity. An expectation maximization (EM) framework is then used to optimize the cost function. Other methods have been developed to estimate tissue lateral displacements [41]. Using a plane strain assumption, the method proposed in [41] exploits the tissue incompressibility principle to generate lateral displacement fields with an improved accuracy and signal-to-noise ratio (SNR). This method assumes small displacements; therefore, the method was later extended to account for larger strains where a nonlinear representation of the strain tensor was used [44]. The algorithm proposed in [45][46], have proposed a linear plane stress inverse elasticity problem formulation to improve the axial and lateral displacements field estimation. Another work presented in [47] has implemented a partial differential equation (PDE) based regularization method coupled with the tissue incompressibility constraint to smooth the displacements fields.

A novel methodology recently proposed for improved strain imaging of the breast, namely, the strain refinement algorithm (STREAL) [42], will be adapted and investigated in this project for enhanced liver elastography. This technique requires an initial estimate of the displacement fields to be processed before it produces an improved estimate of these fields. The displacement fields and strain images are refined by the STREAL technique through smoothing, and then enforcing the fundamental tissue mechanics principles of incompressibility and strain compatibility. Smoothing and incompressibility condition lead to improved displacement fields estimate while the compatibility condition enforcement applies further improvement, leading to the final enhanced strain images.

2.2.3 Young's Modulus Reconstruction

Previous literature proposed various elastic modulus reconstruction techniques. These methods have been formulated based on the premise that soft tissue is considered a Hookean material, behaving like a linear and isotropic material. The inversion techniques based on quasi-static elastography are either direct or iterative. A direct inversion method has been proposed by [48] where the elastic modulus is obtained by solving a linear system obtained by numerical representation of partial differential equations that describe the direct problem for the plane-strain condition. The output elastic modulus image suffered from measurements noise. A more recent work introduced an improved technique where the effect of measurement noise was reduced by computing lateral displacements through adding the tissue incompressibility constraint as described in [41].

The iterative inversion approach developed for Young's modulus reconstruction has been implemented successfully in medical imaging applications. It can generally be viewed as a

parameter optimization problem, where minimization of the error between the measured/estimated and simulated displacements is pursued to find the elastic modulus. The optimization techniques fall under three categories. Firstly, a Hessian-based optimization as described in [49]. As the computational expense to compute the Hessian increases with the increase of parameters, gradient based optimization methods were developed. A gradient based optimization method [50], overcomes the computational limitation of computing the gradient by using an adjoint method to compute the gradient of the objective function.

The third category of pertaining to this approach is founded on using Hooke's law to compute the elastic modulus directly from the measured strain fields. However, as the tissue stress distribution cannot be measured *in-vivo*, previous groups have attempted to estimate it using analytical methods that suffer from substantial idealization errors while being limited to simple organ geometries and tissue distribution. To overcome this limitation, the finite element (FE) method can be used to compute the stress distribution iteratively as described in [51]. A full-inversion-based breast elastography technique was later developed by Samani et al. [52], where the breast Young's Modulus (E) is reconstructed for cancer assessment. This method is applicable to the liver as it was developed assuming that the tissue is linear elastic and isotropic undergoing small deformation. This assumption is valid as the strain induced in the tissue relative to the precompression state can be safely considered infinitesimal. Furthermore, the liver tumor can still be considered linear elastic despite having high collagen content. This is due to the tumor's higher stiffness compared to the healthy tissue which implies even smaller deformation than what is anticipated in the liver healthy tissue during mechanical stimulation. Using Hook's law, the following equation was derived:

$$\frac{1}{E} = \frac{\epsilon_{11}}{\sigma_{11} - \nu\sigma_{22} - \nu\sigma_{33}} \tag{2-2}$$

In this equation E is the tissue Young's modulus and ε and σ denote the tissue strain and stress developed under mechanical simulation, respectively. Also, the indices 1, 2, and 3 represent the three orthogonal space directions and υ is the Poisson's ratio of the tissue. As the tissue was assumed to be a near incompressible material, υ = 0.49 was used. The Young's modulus reconstruction technique proposed in [52] is iterative and it follows a $E^{i+1} = F(E^i)$ recursive formulation in each iteration, where F involves stress calculation using the FE method. Such iterative algorithm is known to diverge unless certain measures are taken. Therefore, their method followed a constrained reconstruction technique, which assumes that E is constant throughout the volume of each of normal and suspicious tissue volumes. Hence, it requires an image segmentation to outline the boundaries of each tissue volume. Although the assumption of tissue elasticity uniformity is reasonably good, the boundaries of tissue volumes, especially those of the tumor, cannot be easily delineated from medical images obtained from ultrasound (US) imaging which is commonly used for real-time elastography. To address these issues, a method was developed by Mousavi et al. with an unconstrained full inversion algorithm for ultrasound elastography [53]. Their strategy involves dividing the finite element model into subsets of n × n finite element windows where the step of averaging E is performed within each window. The axial strain component is commonly acquired in US elastography. As such, the following equation derived from 2D Hooke's law equations of linear elastic and isotropic materials is used for the Young's Modulus reconstruction:

$$\frac{1}{E} = \frac{\epsilon_{11}}{\sigma_{11} - \nu\sigma_{22}} \tag{2-3}$$

Where ε11, σ11, and σ22 are axial strain, axial stress, and lateral stress, respectively. By having a reasonably accurate estimate of ε22 (lateral strain), an equation similar to Equation 2-3 can be used to find another estimate of E. A weighted estimate of the latter can be then combined with the E estimate produced by the axial strain in order to produce a more accurate E image. It is noteworthy that, as the strain is assumed to follow normal distribution, Equation (2-2) calculates (1/E) of each finite element to suppress the noise of the strain through averaging.

Chapter 3

Methodology

3.1 Dataset

3.1.1 Tissue Mimicking Phantom

The imaging data required for the analytical development and evaluation of the methods in this project were acquired from a tissue mimicking phantom elastography phantom (CIRS elastography phantom, Norfolk, VA) that was compressed 0.2 inches axially, resulting in an average strain of 6% [25]. Two ultrasound RF frames were acquired corresponding to the pre- and post-compression states using an Antares Siemens research ultrasound machine (Issaquah, WA, USA) and a VF 10-5 linear array probe with the center and sampling frequencies of 6.67 and 40 MHZ, respectively. The Young's modulus values of the inclusion and the background tissue for the tissue mimicking phantom were 56 kPa and 33 kPa, respectively, leading to a ratio of 1.70.

3.1.2 Liver Cancer Clinical Dataset

A publicly available anonymized dataset of four ultrasound scans acquired (with ERB approval and after receiving informed consent) from four patients who underwent open surgical RF thermal ablation therapy of HCC were used for further evaluation and optimization of the developed methods in this project [26]. The RF ablation procedure was performed using a RITA Model 1500 XRF generator (Rita Medical Systems, Fermont, CA, USA). The ultrasound RF data was acquired using an Antares Siemens research ultrasound machine (Issaquah, WA, USA) and a linear array transducer with a 7.27 MHz center frequency and a sampling rate of 40 MHz. In each scan, the tissue was compressed by the ultrasound probe while ultrasound RF frames were acquired at pre- and post-compression states.

3.2 Enhanced Strain Imaging

A novel methodology recently proposed for improved strain imaging of the breast, namely, the strain refinement algorithm (STREAL) [42], [54], was adapted and investigated in this project for developing a liver elastography technique. This technique requires an initial estimate of the displacement fields to be processed before it produces an improved estimate. The regularized TDE methods of global ultrasound elastography (GLUE) [26]and second order ultrasound elastography (SOUL) [40]were applied separately to obtain the required initial estimates of the tissue axial and lateral displacements fields. A less advanced TDE algorithm, namely dynamic programming and 2D analytic minimization (AM2D) [25] was also investigated to provide initial estimates in order to assess the accuracy of the enhanced displacement and strain fields obtained with low- and high-quality displacement initial guesses combined with the STREAL method.

3.2.1 Initial Displacement Estimation

In this section, the methods mentioned in the previous section to obtain initial displacement fields are described briefly.

3.2.1.1 Dynamic Programming and 2D Analytic Minimization (AM2D)

The input for AM2D is the two ultrasound RF frames pertaining to pre- and post-compression state of the tissue. This method involves minimization of the following regularized cost function:

$$C_s(\Delta\alpha_1, \dots, \Delta\alpha_m,\ \Delta l_1, \dots, \Delta l_m) = \sum_{i=1}^{m}\{[I_1(i,s) - I_2(i + a_i + \Delta a_i,\ s + l_i + \Delta l_i)]^2 + R_A \qquad (3\text{-}1)$$

Where I_1 and I_2 are the pre- and post-compression RF frames of size $m \times n$. Dynamic programming (DP) is used to calculate the initial integer displacements estimates in axial (a_i) and

lateral (l_i) directions for all samples $(i = 1, \dots, m)$ in a single RF line (seed line). The seed RF-line lateral position is indicated by s. R_A represents the following regularization term:

$$R_A = \sum_{i=1}^{m}\{\alpha(a_i + \Delta a_i - a_{i-1} - \Delta a_{i-1})^2 + \beta_a(l_i + \Delta l_i - l_{i-1} - \Delta l_{i-1})^2 + \beta_l'\big(l_i + \Delta l_i - l_{i,s-1}\big)^2 \quad (3\text{-}2)$$

As DP calculates displacements represented by integer number of pixels only, it is not accurate enough to be used in elastography. As such, the regularized cost function is minimized to calculate the subsample $\Delta a_i \; and \; \Delta l_i$ values, which are the subpixel value motion parameters, leading to axial and lateral displacement values at each sample i of the RF line with higher precision. The regularization weight α determines the proximity of axial displacement to its top neighbor. β_a and β_l' determines how close the lateral displacements of each sample should be to its neighbors on top and left. Solving this optimization problem for each axial line independently provides the TDE for all samples of an RF-line. The strain images are calculated using least square regression, over several displacement measurements. In the cost function, which incorporates continuity in both axial and lateral displacements, the regularization coefficients are tuned to adjust the smoothness based on the noise in the input.

3.2.1.2 Global Ultrasound Elastography (GLUE)

Unlike the AM2D method, the GLUE method provides the TDE of all samples within an RF frame simultaneously by optimizing the cost function that incorporates both amplitude similarity and displacement continuity based on first-order spatial derivatives of the displacement filed. Therefore, the cost function formulated in the GLUE method is developed for the entire RF frame:

$$C_g\big(\Delta a_{1,1}, .., \Delta a_{m,n}, \Delta l_{1,1}, \dots, \Delta l_{m,n}\big) = \sum_{j=1}^{n}\sum_{i=1}^{m} D_1\big(i, j, a_{i,j}, l_{i,j}, \Delta a_{i,j}, l_{i,j}\big) + R_g \quad (3\text{-}3)$$

$$D_I(i,j,a_{i,j},l_{i,j},\Delta a_{i,j},\Delta l_{i,j}) = \left[I_1(i,j) - I_2(i + a_{i,j} + \Delta a_{i,j}, j + l_{i,j} + \Delta l_{i,j})\right]^2 \quad (3\text{-}4)$$

$$R_g = \sum_{j=1}^{n}\sum_{i=1}^{m}\{\alpha_1\left(a_{i,j} + \Delta a_{i,j} - a_{i-1,j} - \Delta a_{i-1,j}\right)^2 + \alpha_2\left(a_{i,j} + \Delta a_{i,j} - a_{i,j-1} - \Delta a_{i,j-1}\right)^2 + \beta_1\left(l_{i,j} + \Delta l_{i,j} - l_{i-1,j} - \Delta l_{i-1,j}\right)^2 + \beta_2\left(l_{i,j} + \Delta l_{i,j} - l_{i,j-1} - \Delta l_{i,j-1}\right)^2\} \quad (3\text{-}5)$$

Where C_g is the non-linear cost function, and $a_{i,j}$ and $l_{i,j}$ are the initial displacement fields estimated using DP. These initial estimates are then refined by fine tuning the fields $\Delta a_{i,j}$ and $\Delta l_{i,j}$ obtained by optimizing the cost function. R_g is the regularization term which penalizes the first order derivate of the displacement field. The subscript g refers to GLUE. α_1 ,α_2, β_1, and β_2 denote the axial and lateral continuity weights respectively. Similar to AM2D, the strain images are obtained using least square regression on the displacement measurements.

3.2.1.3 Second Order Ultrasound Elastography (SOUL)

As described in the previous chapter, the SOUL method differs from the GLUE by incorporating a second-order regularization term in addition to the first-order derivative regularizer in the cost function, leading to:

$$C(\Delta\alpha_{1,1},\ldots..,\Delta a_{m,n},\Delta l_{1,1},\ldots,\Delta l_{m,n}) = \sum_{j=1}^{n}\sum_{i=1}^{m} D_I(i,j,a_{i,j},l_{i,j},\Delta a_{i,j},\Delta l_{i,j}) + R_s \quad (3\text{-}6)$$

Where R_s is the regularization term as follows:

$$R_s = \sum_{j=1}^{n}\gamma\left[\alpha_{1,j} + \Delta\alpha_{1,j}\right]^2 + R_1 + R_2 \quad (3\text{-}7)$$

The first part of the regularization term imposes a first-order regularizer on the first sample of each RF-line, assuming an imaginary initial sample exhibiting zero displacement. The spatial regularization weight γ is for the initial samples, while R_1 and R_2 are the first and second continuity terms, respectively. The first-order term minimizes the first derivative of the displacements

between two adjacent points to suppress noise. The second order constraint align with the tissue deformation physics, enforcing continuity on strain. Combined with the first-order term, the second-order derivative-based regularizer further enhances the displacement field smoothness, as the first-order continuity constraint by itself is not enough representation of the tissue deformation mechanics.

3.2.2 Strain Refinement Algorithm (STREAL)

As mentioned before, the STREAL method [42] requires an initial displacement estimate. In the method's implementation introduced in [43], the initial estimate was obtained by processing a pair of RF data frames using the [25] GLUE method [26]. In this work, we explored the AM2D, GLUE, and the SOUL methods [40] to generate the displacement fields' initial estimates used with the STREAL method. The STREAL method includes three steps of smoothing the displacement fields, enforcement of tissue incompressibility principle, and enforcement of strain compatibility condition [42].

The smoothing step is performed through a Laplacian filtering on the displacement field where the Laplacian is a 2D isotropic operator consisting of the second spatial derivates of the field. Minimization of the Laplacian norm is carried out to smooth the displacement field while ensuring its continuity. For this purpose, Tikhonov regularization is used which leads to the following least squares solution:

$$U_{new} = (I + \lambda^2 L^T L) U_m \tag{3-8}$$

where L is the finite difference approximation of the Laplacian operator. The regularization weight coefficient λ is used to determine the smoothness while still maintaining the proximity to the

original (initial) displacement field. The L-curve technique [55] was used to find the optimal value of λ.

Enforcing tissue incompressibility is the second step where it is expressed mathematically using the following equation:

$$\nabla . U(x,y,z) = \frac{\partial u_x}{\partial x} + \frac{\partial u_y}{y} + \frac{\partial u_z}{\partial z} = 0 \tag{3-9}$$

Here the displacement field divergence is set to zero. The *x*, *y*, and *z* correspond to the lateral, axial, and out-of-plane directions respectively. However, US imaging does not provide the out-of-plane displacement information. While previous methods have used the plane-strain and plane-stress conditions to enforce incompressibility, STREAL considers 3D tissue deformation approximated by the Boussinesq's model to estimate the out-of-plane strain analytically.

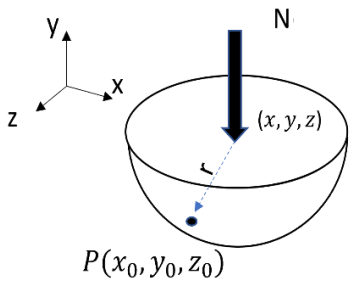

Figure 3-1. A representation of a semi-infinite medium under a point load.

Figure 3-1 shows (x_0, y_0, z_0) and (x, y, z) which are the coordinates of an arbitrary point P and loading point, respectively. Using the equations (3-10), (3-11) and (3-12), the axial, lateral and out-of-plane stresses can be calculated.

$$\sigma_{xx} = \frac{0.5N}{\pi}\left\{\frac{3(y_0-y)(x_0-x)^2}{r^5} - (1-2v)\left[\frac{(x_0-x)^2-(z_0-z)^2}{r(r^2-(y_0-y)^2)(r+(y_0-y))} - \frac{\left((z_0-z)^2(y_0-y)\right)}{(r^2(r^2-(y_0-y)^2))}\right]\right\} \tag{3-10}$$

$$\sigma_{yy} = \frac{1.5N}{\pi}\ \frac{(y_0-y)^2}{r^5} \tag{3-11}$$

$$\sigma_{zz} = \frac{0.5N}{\pi}\left\{\frac{3(y_0-y)(z_0-z)^2}{r^5} - (1-2v)\left[\frac{(z_0-z)^2-(x_0-x)^2}{r(r^2-(y_0-y)^2)(r+(y_0-y))} - \frac{\left((x_0-x)^2(y_0-y)\right)}{\left(r^2(r^2-(y_0-y)^2)\right)}\right]\right\} \quad (3\text{-}12)$$

For calculating the stresses induced by pushing a US transducer, equations (3-10), (3-11) and (3-12) are integrated over the surface of the transducer. Using these stresses, axial and out-of-plane strains are calculated using Hooke's law where the tissue Young's modulus and Poisson's ratio are required. In our implementation, we assume the liver is linear elastic with a Young's modulus value of 700 Pa and Poisson's ratio of 0.49. As indicated earlier, this assumption is valid given the small deformation anticipated relative to the tissue's precompression state. Using the resulting out-of-plane and axial strains, their ratio (K) at each point can be obtained, leading to the following form of the incompressibility equation.

$$\frac{\partial u_x}{\partial_x} + (K+1)\frac{\partial u_y}{\partial y} = 0 \quad (3\text{-}13)$$

The displacement fields obtained after smoothing in the first step are combined with the finite difference approximation of Equation (3-13) to lead to the following matrix equation:

$$\begin{bmatrix} C \\ I \end{bmatrix} U = \begin{bmatrix} 0 \\ U_m \end{bmatrix} \rightarrow AU = b \quad (3\text{-}14)$$

Here, U contains the lateral and axial displacements, and C is a matrix containing coefficients of the finite difference approximation of Equation (3-13). U_m is the displacement field obtained from the first step and the solution U is the improved displacement field. Equation (3-14) is solved using the Polak-Ribiere conjugate gradient method [56].

The last step produces a refined estimate of the strain by enforcing the tissue strain compatibility condition. The equation governing strain compatibility in terms of the strain tensor components is given as:

$$\frac{\partial^2 \varepsilon_{xx}}{\partial y^2} + \frac{\partial^2 \varepsilon_{yy}}{\partial x^2} = 2\frac{\partial^2 \varepsilon_{xy}}{\partial x \partial y} \tag{3-15}$$

The finite difference method can be used to derive a numerical approximation for equation (3-15), leading the following matrix equation:

$$P\varepsilon = 0 \tag{3-16}$$

where ε is a vector containing axial, lateral, and shear strains, and P is the matrix containing the parameters of the finite difference approximation of the compatibility equation. Combined with the strains calculated based on the refined displacements obtained in the previous step, the following system of equations can be obtained where ε_m are the strains computed using the previous step's displacements. Equation (3-17) can be solved using the Polak-Ribiere method to obtain a further refined estimate of the strain.

$$\begin{bmatrix} P \\ I \end{bmatrix} \varepsilon = \begin{bmatrix} 0 \\ \varepsilon_m \end{bmatrix} \rightarrow B\varepsilon = e \tag{3-17}$$

3.3 Full Inversion Based Elastic Modulus Reconstruction

We adapted the methodology presented in [53] for breast elastography to reconstruct the relative Young's modulus images of the liver. For the iterative finite element (FE) analysis in this method, the ultrasound field of view (FOV) was uniformly meshed using rectangular elements. Our implementation of the algorithm is summarized as follows:

1. Using an initial Young's modulus distribution, which can be a uniform distribution, the stress field is computed using 2D finite element (FE) analysis.
2. Using the axial and lateral strains obtained from the methods described in the previous subsection, the Young's modulus reciprocal value of each element in the FE model of the tissue FOV is calculated using the following equations:

$$\frac{1}{E_{11}} = \frac{\epsilon_{11}}{\sigma_{11} - \nu\sigma_{22}}, \quad \frac{1}{E_{22}} = \frac{\epsilon_{22}}{\sigma_{22} - \nu\sigma_{11}} \tag{3-18}$$

3. The reciprocal of E values obtained through axial and lateral strains are assigned weights (with higher weights given to the axial strains) before they are combined to obtain a more accurate E reciprocal estimate.
4. The average Young's modulus reciprocal value of each n×n element window within the FE model is assigned to all elements in the window.
5. The updated Young's modulus of each element is obtained by inverting the E reciprocal obtained from Step 4.
6. To obtain a smooth distribution of the Young's modulus values, a Gaussian smoothing filter is used.
7. Returning to Step 1 with the updated Young's modulus distribution and continuing the iterative procedure until the difference between two consecutive E values for all FE elements is less than 0.002.

In Equation (3-18), ε and σ correspond to the tissue strain and stress, respectively. The indices 11 and 22 represent axial and lateral directions, respectively. The tissue Poisson's ratio, ν, was set to 0.49 as the liver tissue is assumed to be near incompressible. The size of the n×n averaging window mentioned in Step 4 was set to 3×3. For the reconstruction algorithm, the FE model of the US FOV, which was mentioned in Step 1, uses the plane stress assumption. This was decided based on the results of the *in-silico* experiment described in the following section. In the finite element model of the US FOV, the boundary nodal points were assigned boundary conditions based on the displacements obtained using the methods presented in section 3.2. The flowchart of the proposed method is shown in Figure 3-2.

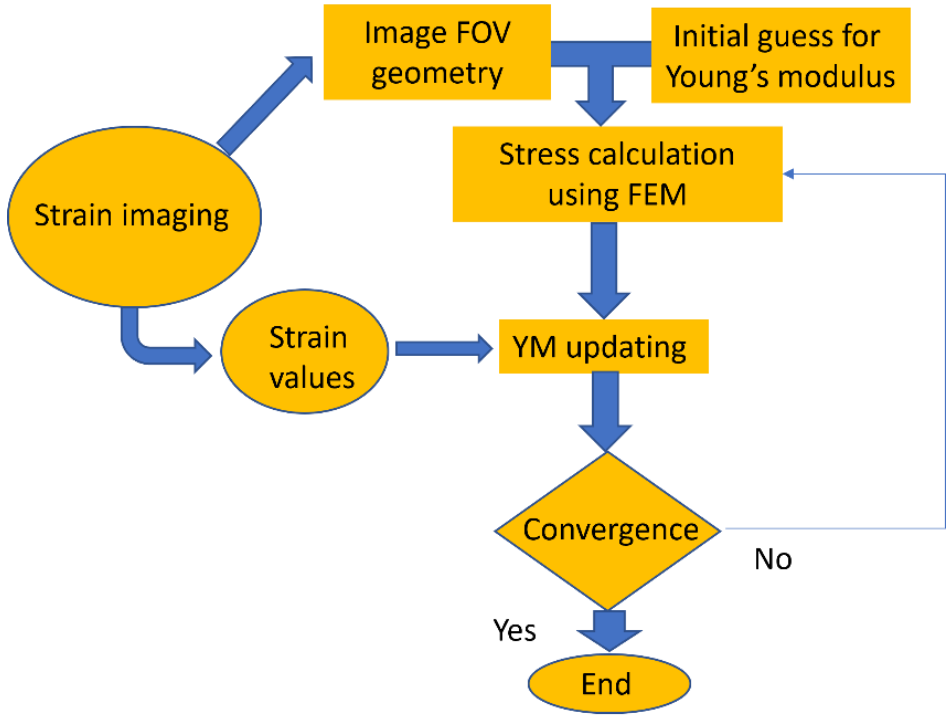

Figure 3-2 Flow chart demonstrating the unconstrained E reconstruction algorithm.

3.4 3D Finite Element Models of the Liver for Simulation Analysis

The first step of Young's modulus reconstruction technique outlined in the previous section involved FE analysis of a 2D model approximating the actual liver's 3D geometry. The 2D FE model represents the US FOV and two model options are available to approximate the 3D model for the FE analysis: the plane stress and plane strain models. To assess and compare the accuracy of the 2D plane stress and plane strain finite element models of the liver compared to the associated ground truth 3D model, a set of *in-silico* experiments of liver USE was conducted using the ABAQUS finite element solver (ABAQUS 2019, Dassault Systèmes Simulia Corp., Johnston, RI, USA). For this purpose, a liver model was derived from a liver CT image to be used in the experiment.

The 3D liver model shown in Figure 3-3 was created after segmenting the liver in an abdominal CT image acquired from a hepatocellular carcinoma patient [57][58], using 3D slicer [59], [60]. The output was first made smoother and initially meshed using Autodesk Meshmixer to improve the quality of the model. Hypermesh (CAE Altair HyperWorks, Altair Engineering, Inc., Troy MI, USA) was then used to generate a 3D FE mesh consisting of tetrahedral elements. The US probe's 3D model was designed using Abaqus, based on the dimensions of the probe used in the clinical study.

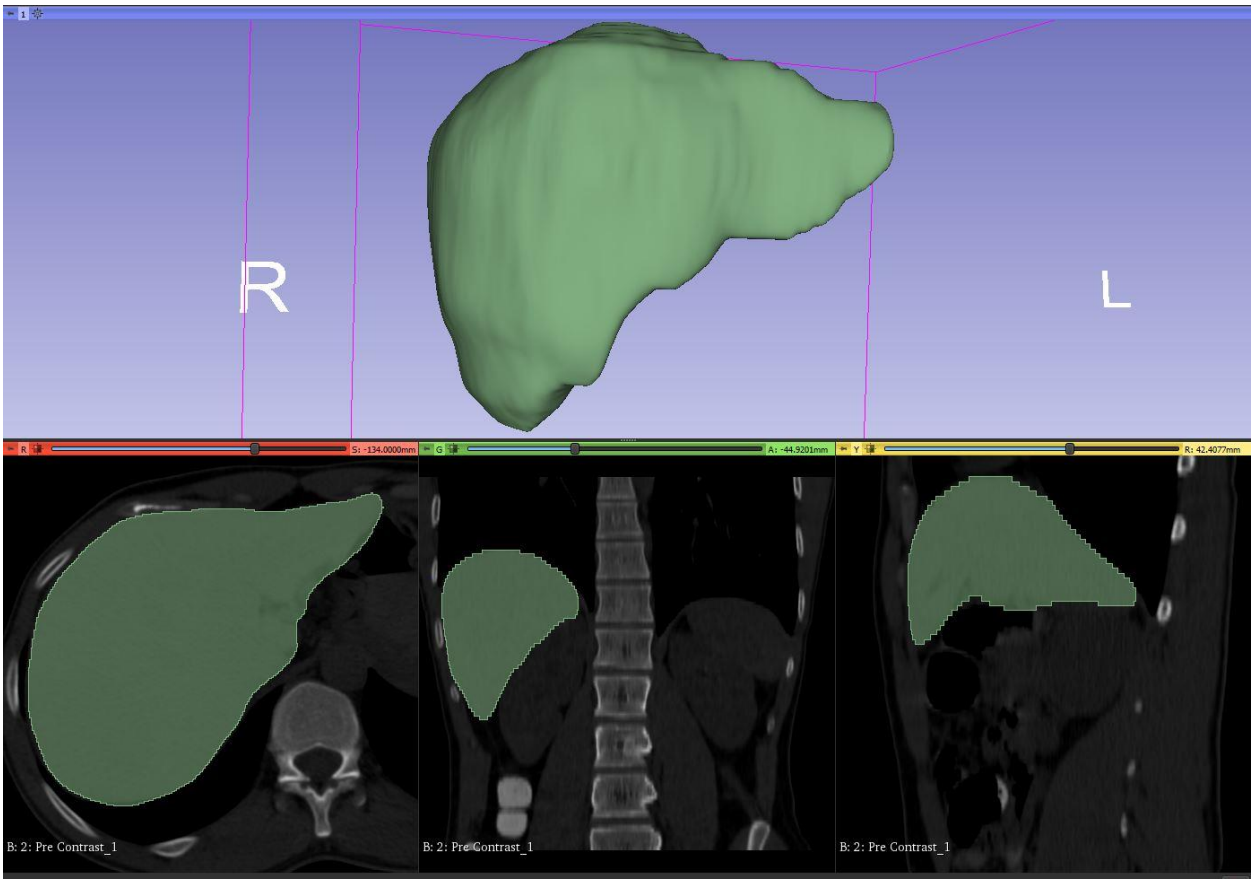

Figure 3-3. Segmented liver from the volumetric CT image and the created 3D model.

Contact mechanics was used for the FE analysis where a master-slave formulation was implemented in ABAQUS. To improve the simulation realism, the contact problem was carried out in two steps. In the first step, the probe was lowered onto the liver model until the transducer was in full contact

with the surface. The second step involved further quasi-static compression of approximately 3-mm to achieve the desired deformation. In this *in-silico* study, we simulated three different scenarios with different probe positions as shown in Figure 3-4.

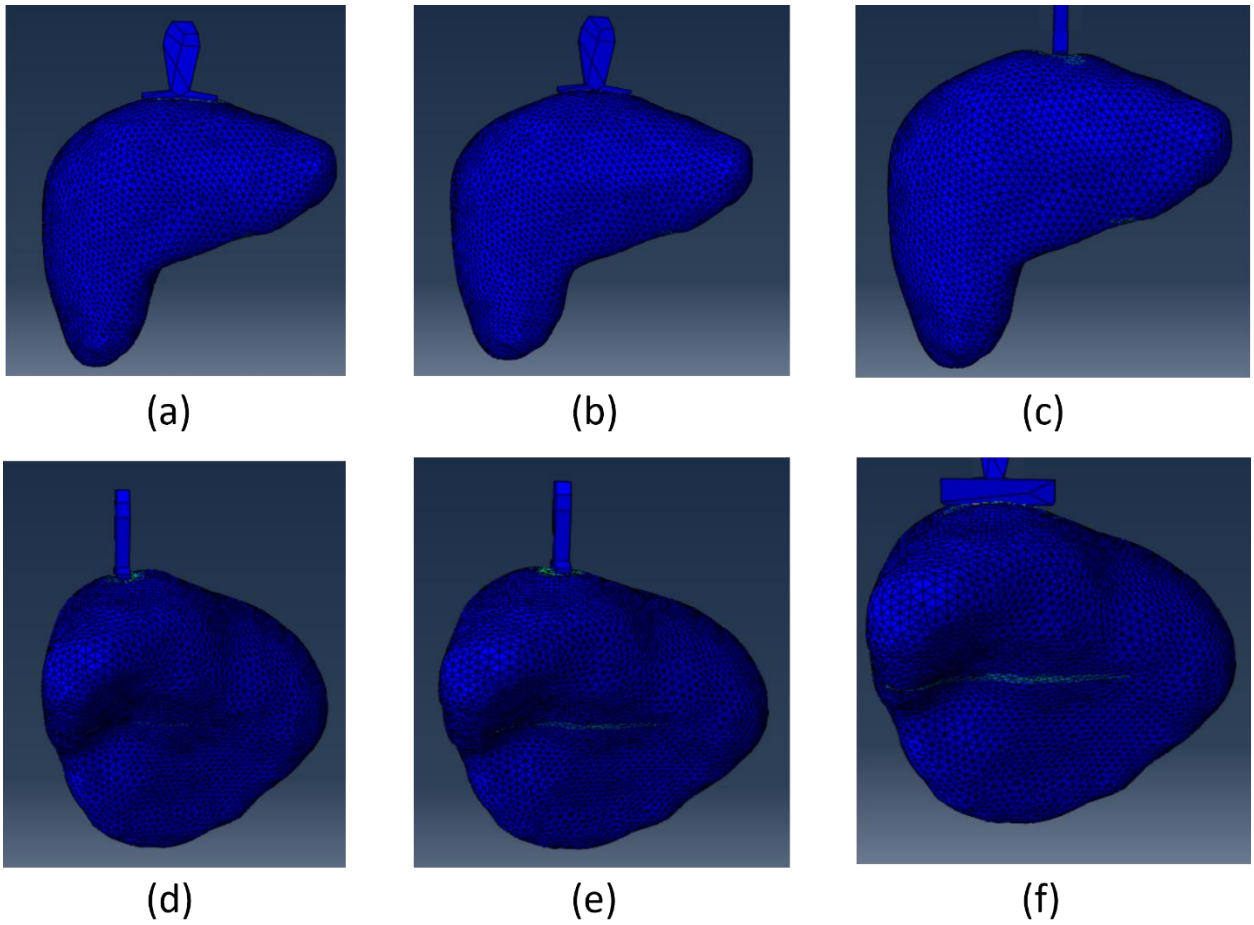

Figure 3-4. Liver and probe 3D models in contact. Top row shows the front view of the three orientations (a-c), while the bottom row shows the side view of the three orientations (d-f).

The 3 positions are chosen to mimic the intra-operative ultrasound monitoring done through open surgical ablation procedures for liver cancer. Selected elements of the liver are chosen to mimic the shape and size of a liver tumor with a cross section located beneath the probe as shown in Figure 3-5. The Young's modulus of the elements representing the healthy liver tissue was set to 700 Pa while the Young's modulus of the elements representing the tumor was set to 3 KPa [18]. The

probe's Young's modulus was set to a very high value (3000KPa) to represent a rigid material that deforms the liver during the contact process. The Poisson's ratio was set to 0.49 to represent an incompressible material for all parts of the model.

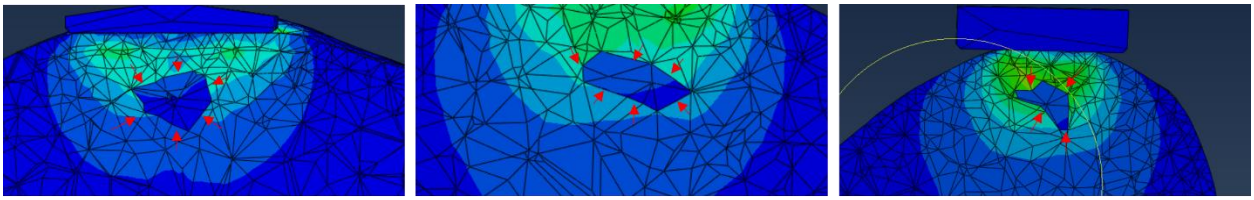

Figure 3-5. Cross-section of chosen elements inside the liver model that represent the tumor shapes. The tumor region is shown using red arrow heads.

The 3D nodal displacements were extracted after each simulation and imported into MATLAB (MATLAB, 2021a, Natick, Massachusetts: The MathWorks Inc.). We defined a set of 306×268 nodes which represents the US 2D FOV as shown in Figure 3-6. For each probe position, the node set representing the US FOV was used to interpolate the nodal displacements corresponding to the ones extracted from the associated 3D simulation. These interpolated displacements were then used for comparison to the displacements obtained from the 2D FE model (within the 2D plane).

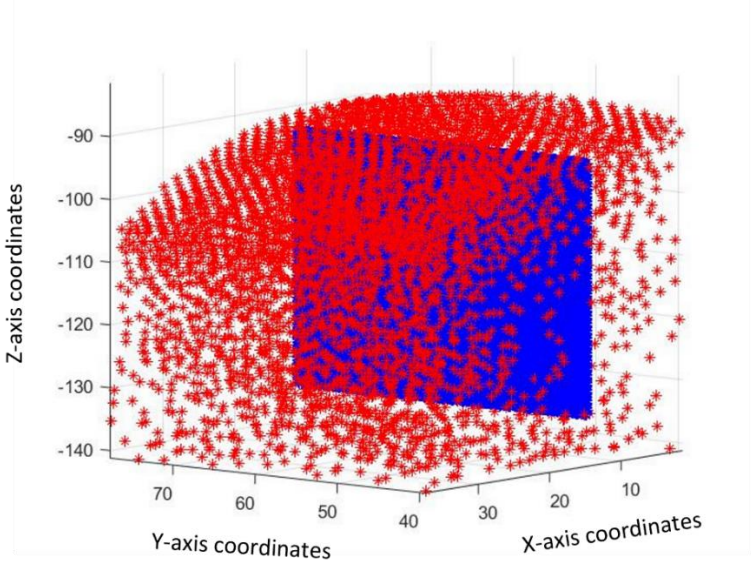

Figure 3-6. Orientation of the US FOV (shown in blue) aligned within the liver model (FE nodes are shown in red) after deformation.

The FE mesh of 2D planes (US FOV) modelled in ABAQUS contained 306×268 nodes while the elements' mechanical properties were consistent with those of the 3D model. The 2D models were created with tumor shapes corresponding to the tumor shapes from the 3D model in the US imaging plane. We used the displacements obtained from the 3D model (ground truth) to find the nodal displacements on the boundaries of US FOV before using them as prescribed boundary conditions to deform the 2D planes during simulation. For each case, FE analyses were conducted with the FOV elements set to 2D plane stress or plane strain element types. Figure 3-7 shows the FE mesh of US FOV and the displacement field obtained from FE simulation of the FOV undergoing the prescribed boundary conditions where plane stress model was used. The displacements generated for each case were extracted and compared to the ground truth displacements using normalized mutual information (NMI) which was calculated using the following equation:

$$NMI = \frac{(H_x + H_y)}{H_{xy}} \tag{3-19}$$

where H_x and H_y are the marginal entropies for the displacement images obtained from the 2D models and the 3D ground truth model, respectively. H_{xy} is the joint entropy of the two images. The displacement values in each image were quantized uniformly into 256 bins before generating the histograms to estimate the marginal and joint entropies.

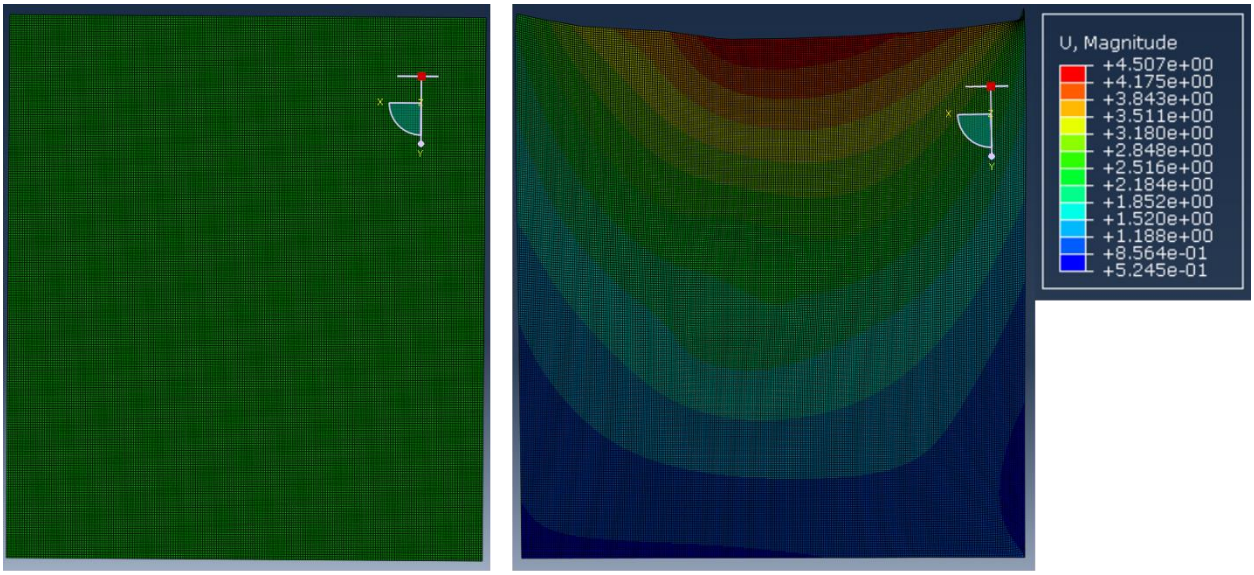

(a) (b)

Figure 3-7. The finite element mesh of the 2D plane (US FOV) before (a) and after (b) after applying prescribed boundary conditions, where the displacement field obtained using plane stress model has been shown.

3.5 Evaluation

To evaluate the strain enhancement and the reconstructed E image, the proposed method was applied to a tissue mimicking phantom and data sets pertaining to four liver cancer patients. In the tissue mimicking phantom study, we first calculated the ratio of the average Young's modulus value of the inclusion to the average Young's modulus value of the background and compared them to their respective true values. The method was evaluated qualitatively by generating the strain and E images and comparing the lesion region between the proposed method and other state of the art methods. The unitless metrics signal-to-noise ratio (SNR) and contrast-to-noise ratio (CNR) were used to quantitatively compare the results according to the following equations.

$$CNR = \frac{C}{N} = \sqrt{\frac{2(\bar{S}_b - \bar{S}_t)^2}{\sigma_b^2 + \sigma_t^2}}, SNR = \frac{\bar{S}}{\sigma} \tag{3-17}$$

where $\overline{s_t}$ and $\overline{s_b}$ are the spatial strain average of the target and background, σ_t^2 and σ_b^2 are the spatial strain variance of the target and background, and $\bar{S}$ and σ are the spatial average and

variance of a window in the strain image, respectively. The SNR and CNR are calculated for the results using windows, which are located in approximately uniform regions, and therefore, respective strain is expected to be relatively constant within each window. The distribution of the target and background values in the strain and the E images is fitted to a Gaussian distribution to compare the standard deviation of the values among the methods being evaluated.

Chapter 4

Results

In this chapter, we first compare the performance of existing TDE-based tissue displacement estimation methods to the original STREAL method which utilizes initial displacement estimates produced by the GLUE method. Afterwards, the power of STREAL in producing an enhanced strain image by using initial displacement estimates generated using different TDE methods will be assessed. The tunable parameters for the TDE methods were set using the empirically optimized values reported in the literature [26], [40], [61]. Specifically, the tunable parameters used for the AM2D algorithm were set to $\alpha = 5$, $\beta_a = 10$, $\beta_l = 0.005$, and $T = 0.2$. As for the GLUE and SOUL algorithms, the parameters were set to $\alpha_1 = 5$, $\alpha_2 = 1$, $\beta_1 = 5$, and $\beta_2 = 1$ in the phantom experiments. As for the clinical cases, α_1 *and* β_1 in the GLUE and SOUL algorithms were set to 20, because of higher level of noise in the RF data. In the SOUL algorithm, the second-order regularization parameters, namely $\{\theta_1, \theta_2, \lambda_1, \lambda_2\}$, were set as multiples of the first order weights $\{\alpha_1, \alpha_2, \beta_1, \beta_2\}$. The multiplying factor was tuned to 500, and γ was set to 0.1 in all experiments. The DP parameter was set to $\alpha_{DP} = 0.15$ for all algorithms.

In Figure 4-1, the top row illustrates the B-mode scans pertaining to the phantom and clinical studies data, while the bottom row shows the CT scans obtained from the patients after the RF ablation therapy. Figure 4-2 shows the windows used for SNR and CNR calculation. The windows chosen to represent the target (tumor/inclusion) and the background areas are rectangular. They were chosen to encompass uniform areas that best represents the target and the background.

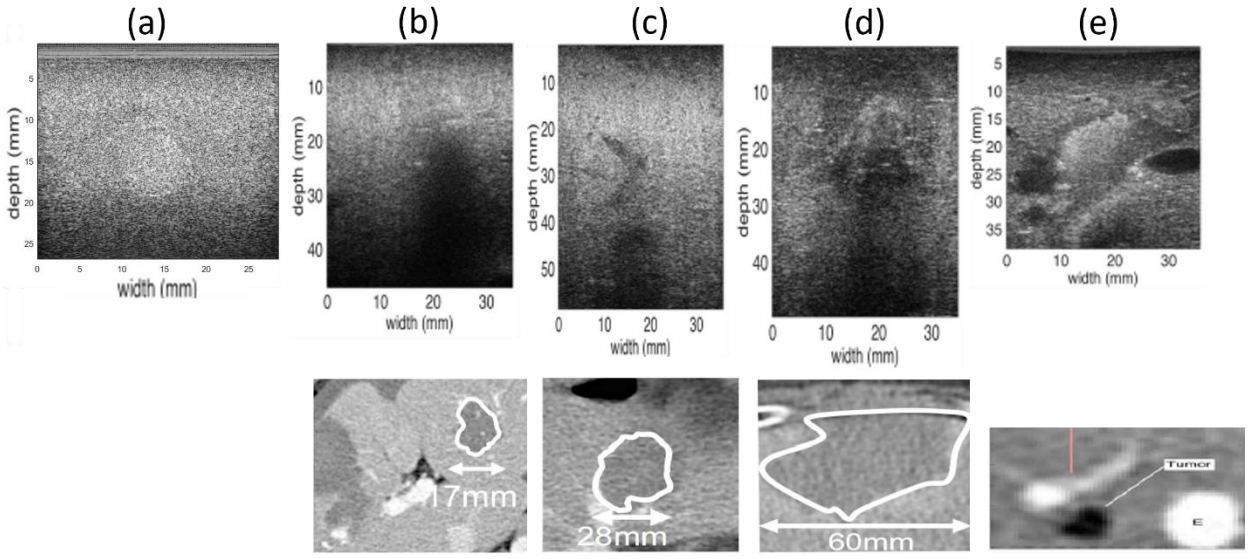

Figure 4-1. Top row shows B-mode images of the tissue mimicking phantom cases. Bottom row shows acquired CT images of the liver where ablated regions are delineated [26]. Columns (a) shows the phantom, (b) patient 1, (c) patient 2, (d) patient 3, and (e) patient 4.

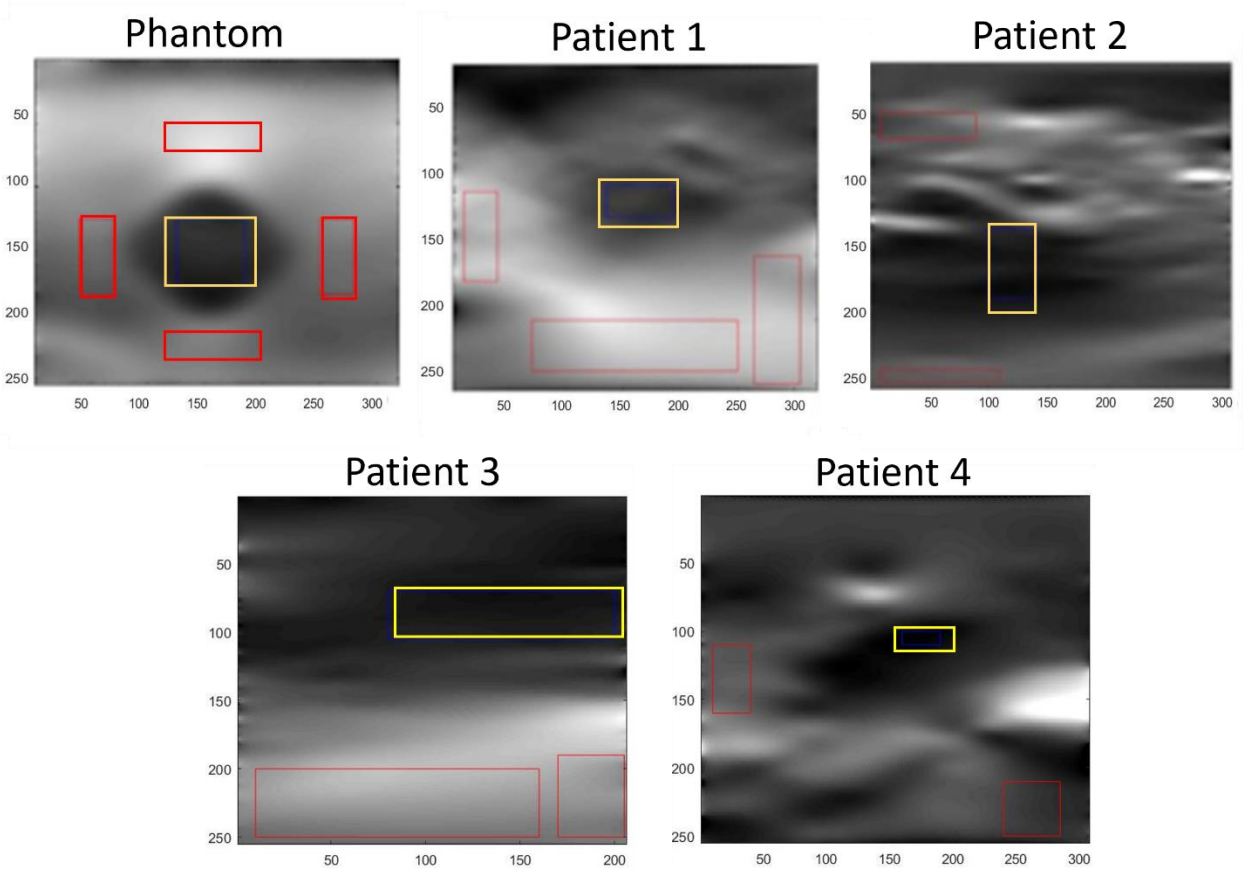

Figure 4-2. Windows used for SNR and CNR calculations, where the yellow and red windows indicate the target and background areas, respectively.

4.1 Enhanced Strain Image Generation

Figures 4-3, 4-4, 4-5, 4-6, and 4-7 show the axial and lateral displacement and strain images produced using the GLUE, Original STREAL, and SOUL methods for the tissue-mimicking phantom and clinical liver cancer cases. The top two rows in these figures show the generated axial and lateral displacement images, respectively. The displacement images are relatively similar across all the methods. The bottom row shows the lateral strain images obtained using GLUE, SOUL and STREAL methods. Compared to the lateral strain images obtained from the GLUE and SOUL methods, the enhanced images generated by the STREAL method are less noisy while they show better consistency with the tumor outline which was delineated manually. This higher consistency is more obvious in Figures 4-4 and 4-7. STREAL method produced better lateral strain images where the improvement in the lateral strain shown in Figures 4-4 (c) and 4-7 (c) is more remarkable.

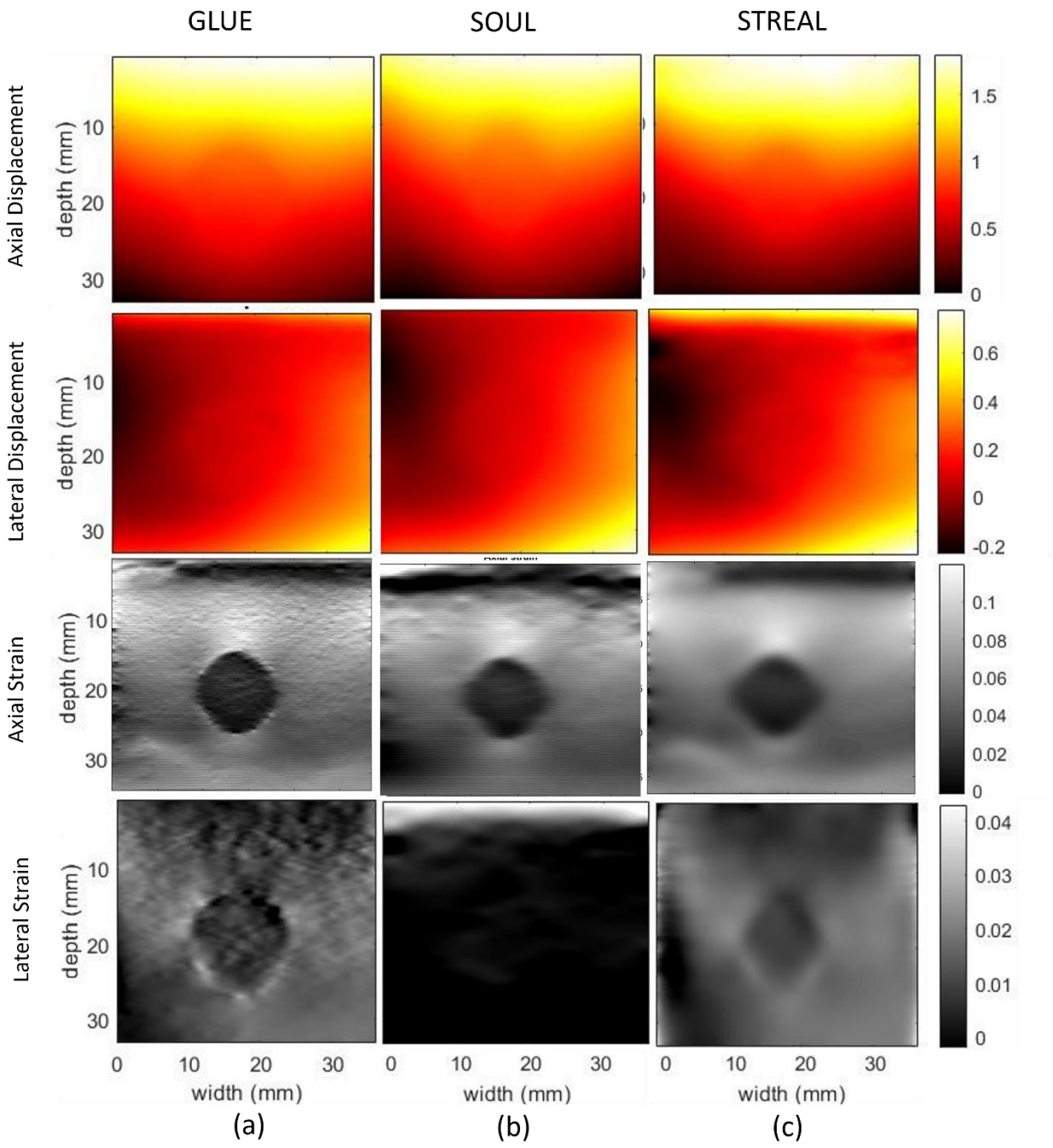

Figure 4-3. Images generated using the (a) GLUE, (b) SOUL, and (c) STREAL methods for the tissue-mimicking phantom case study.

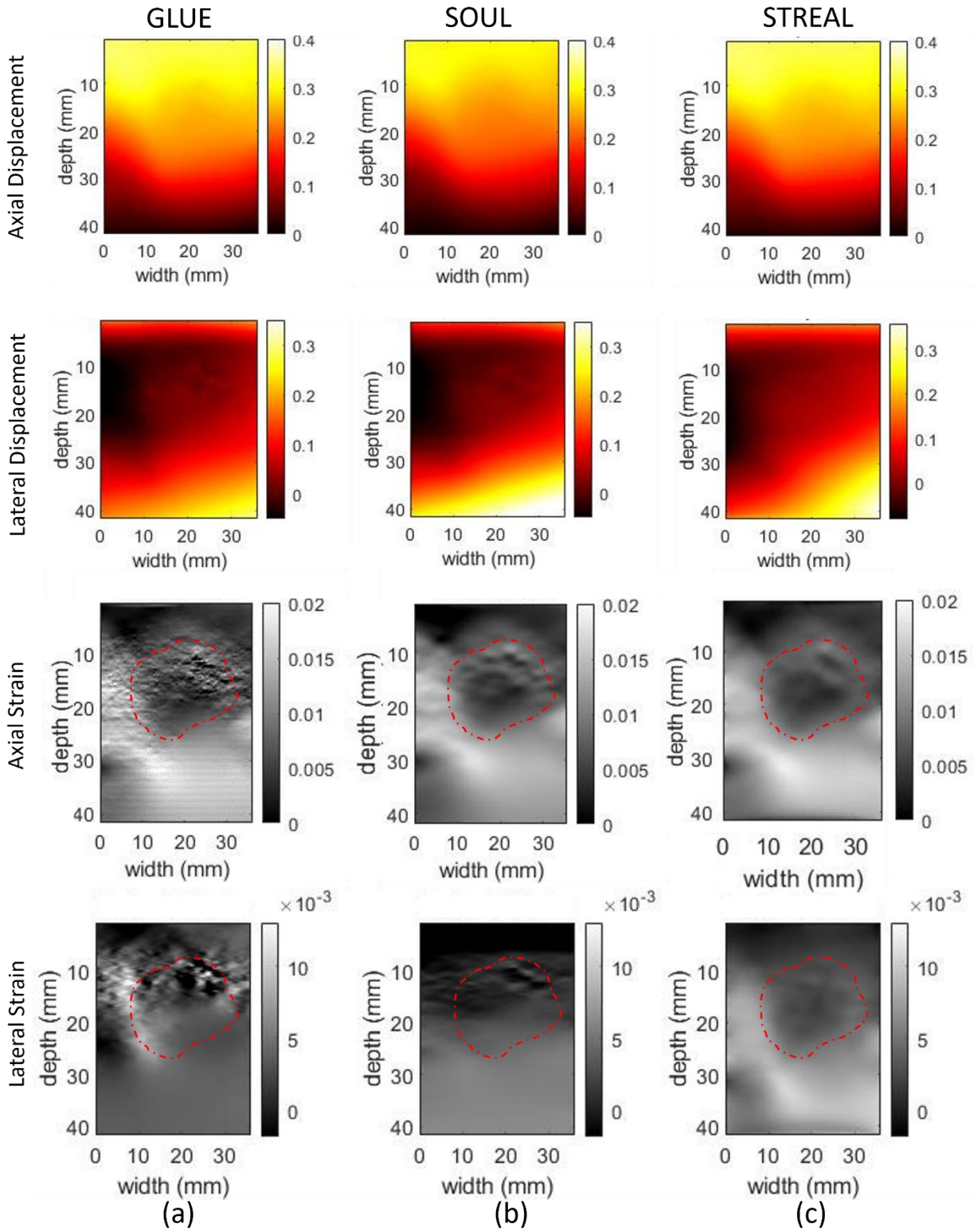

Figure 4-4. Displacement and strain images generated for patient 1 using the (a) GLUE, (b) SOUL, and (c) STREAL methods. The tumor region in each image is delineated with red dashed line.

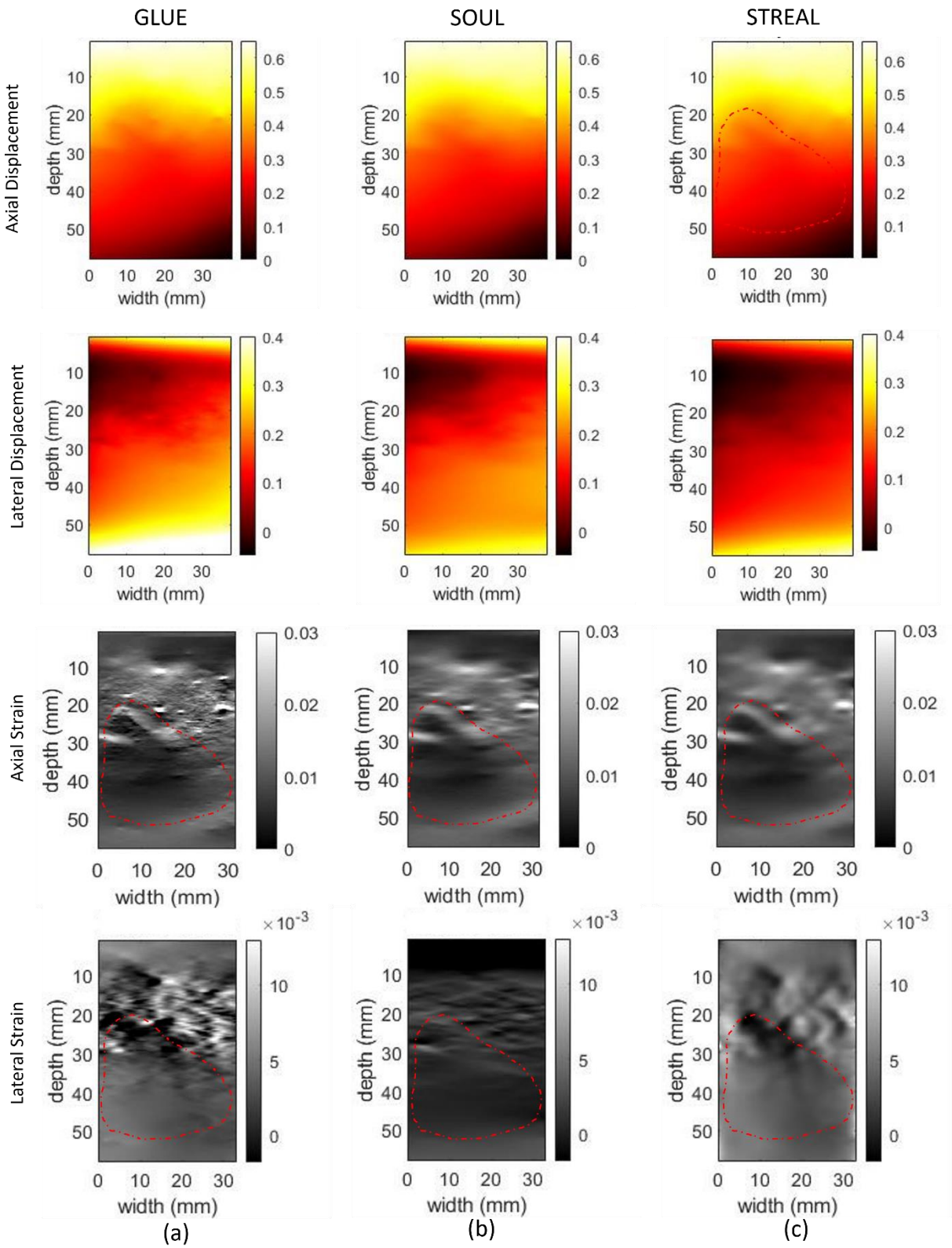

Figure 4-5. Displacement and strain images generated for patient 2 using the (a) GLUE, (b) SOUL, and (c) STREAL methods. The tumor region in each image is delineated with red dashed line.

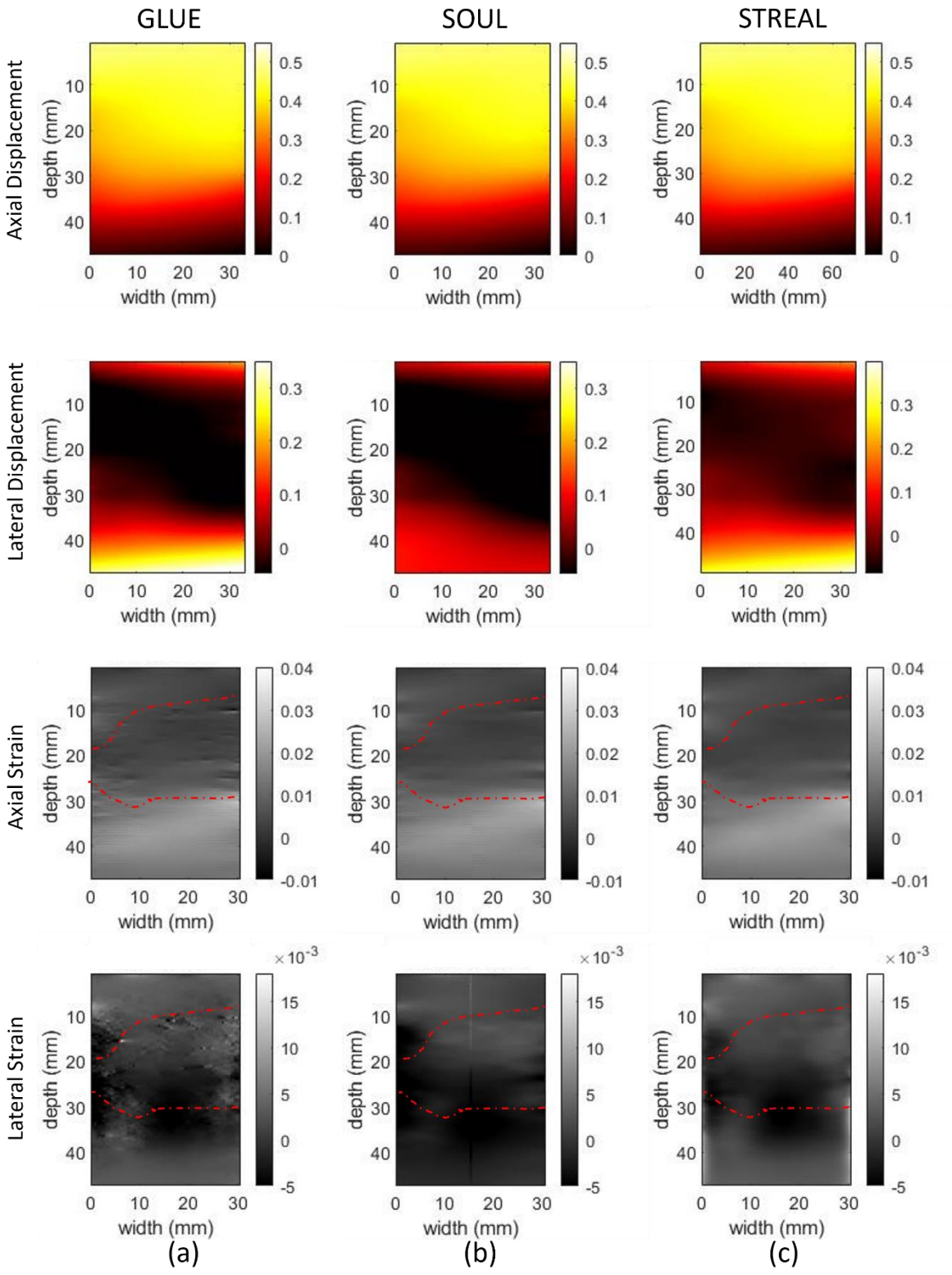

Figure 4-6. Displacement and strain images generated for patient 3 using the (a) GLUE, (b) SOUL, and (c) STREAL methods. The tumor region in each image is delineated with red dashed line.

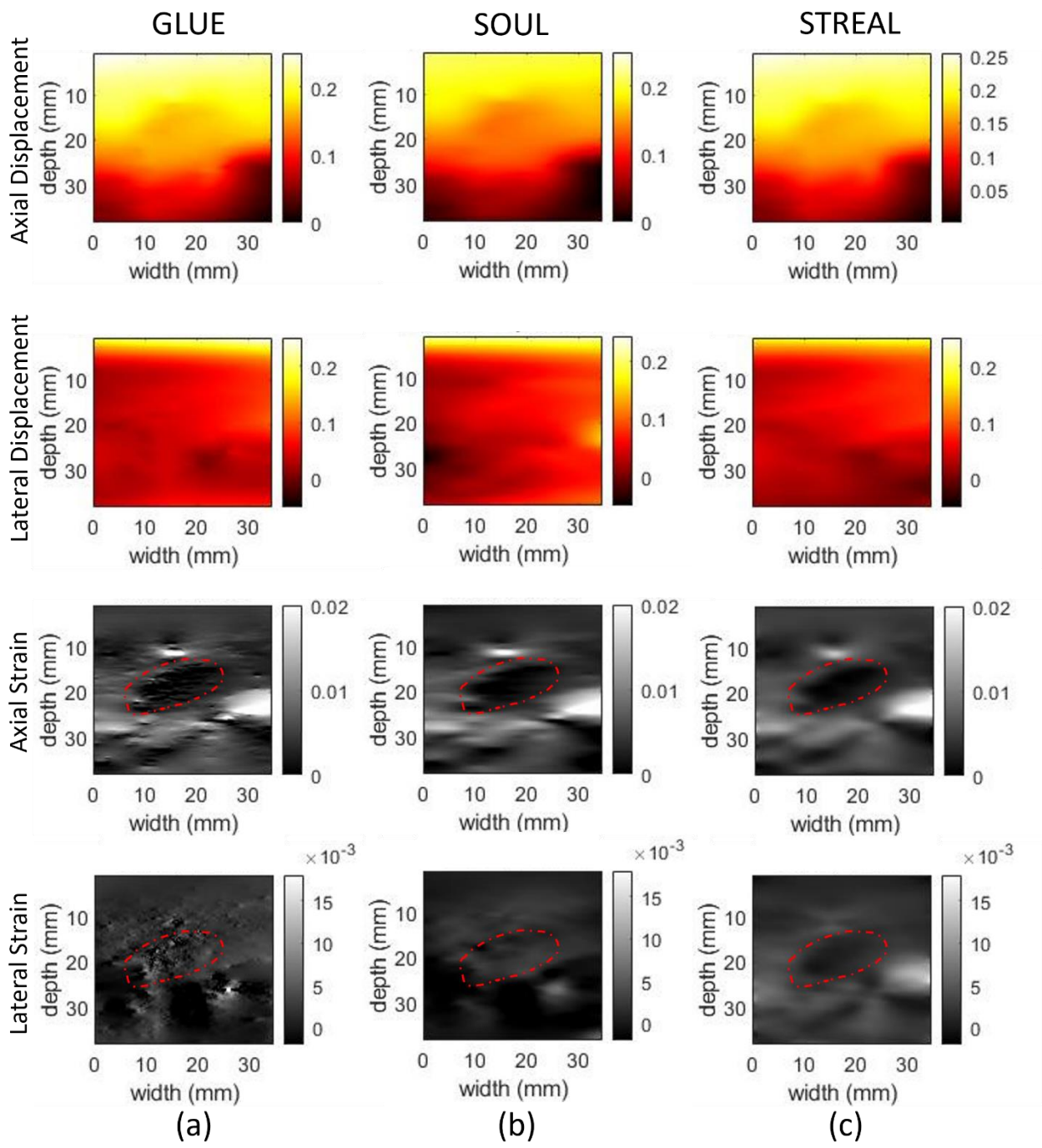

Figure 4-7. Displacement and strain images generated for patient 4 using the (a) GLUE, (b) SOUL, and (c) STREAL methods. The tumor region in each image is delineated with red dashed line.

Table 4-1. SNR and CNR values pertaining to the axial strain images of the phantom and clinical cases. The highest values in each row have been shown in bold font.

Data	SNR			CNR		
	GLUE	**SOUL**	**STREAL**	**GLUE**	**SOUL**	**STREAL**
Phantom	27.44	27.66	**29.47**	18.18	21.34	**27.09**
Patient 1	21.13	17.35	**26.22**	14.77	16.78	**25.95**
Patient 2	13.11	14.64	**22.53**	12.84	14.25	**21.34**
Patient 3	14.95	19.07	**22.4**	15.76	14.90	**20.61**
Patient 4	14.80	12.84	**21.98**	14.90	13.53	**25.33**

Table 4-2 Standard deviation of the strain values in the chosen target and background areas of the phantom case. The lowest values in each row have been shown in bold font.

Phantom	Axial Strain			Lateral Strain		
	GLUE	**SOUL**	**STREAL**	**GLUE**	**SOUL**	**STREAL**
Target	0.012	0.010	**0.008**	0.0077	0.0056	**0.0031**
Background	0.0138	0.0162	**0.0129**	0.0078	0.0071	**0.0047**

The calculated SNR and CNR values pertaining to axial strain images of the tissue mimicking phantom and the clinical cases generated using GLUE, SOUL, and the original STREAL methods are presented in Table 4-1. This table shows that the STREAL method produces the highest SNR and CNR values, outperforming the other two methods across the datasets used in this work. Table 4-2 presents the standard deviation of strain values within the target and background areas of the phantom case. The results in this table show that the strain images produced by the STREAL method have the lowest standard deviation in both the target and background regions, demonstrating better consistency with the distribution of the homogenous materials in the phantom. This implies higher precision in the strain fields generated by the STREAL method through applying Laplacian filtering and imposing the tissue incompressibility and strain compatibility constraints. In contrast to the phantom background and inclusion parts that can be safely regarded as homogenous, the background and tumor liver tissue involved in the clinical cases is expected to have some degree of heterogeneity. As such, the standard deviation comparison was only performed in the phantom case.

Figure 4-8 illustrates the phantom results produced using the STREAL method where different initial displacement estimates obtained using the DP, AM2D, SOUL and GLUE methods were applied. The enhanced axial and lateral displacement images shown are very similar across all methods except those produced using the initial displacement fields obtained from the DP method. The latter strain images are illustrated in column (a), where image distortion is more remarkable compared to the other methods. Therefore, using the DP method to obtain initial estimates of displacement was only investigated for the phantom case. However, as shown in column b of Figure 4-8, when the AM2D method was used to obtain the initial displacement estimate, compared to images produced with initial guesses obtained from the GLUE and SOUL methods, better axial and lateral strain fields with clearer symmetry around the centerline of the phantom, which is anticipated from the phantom mechanics, were obtained.

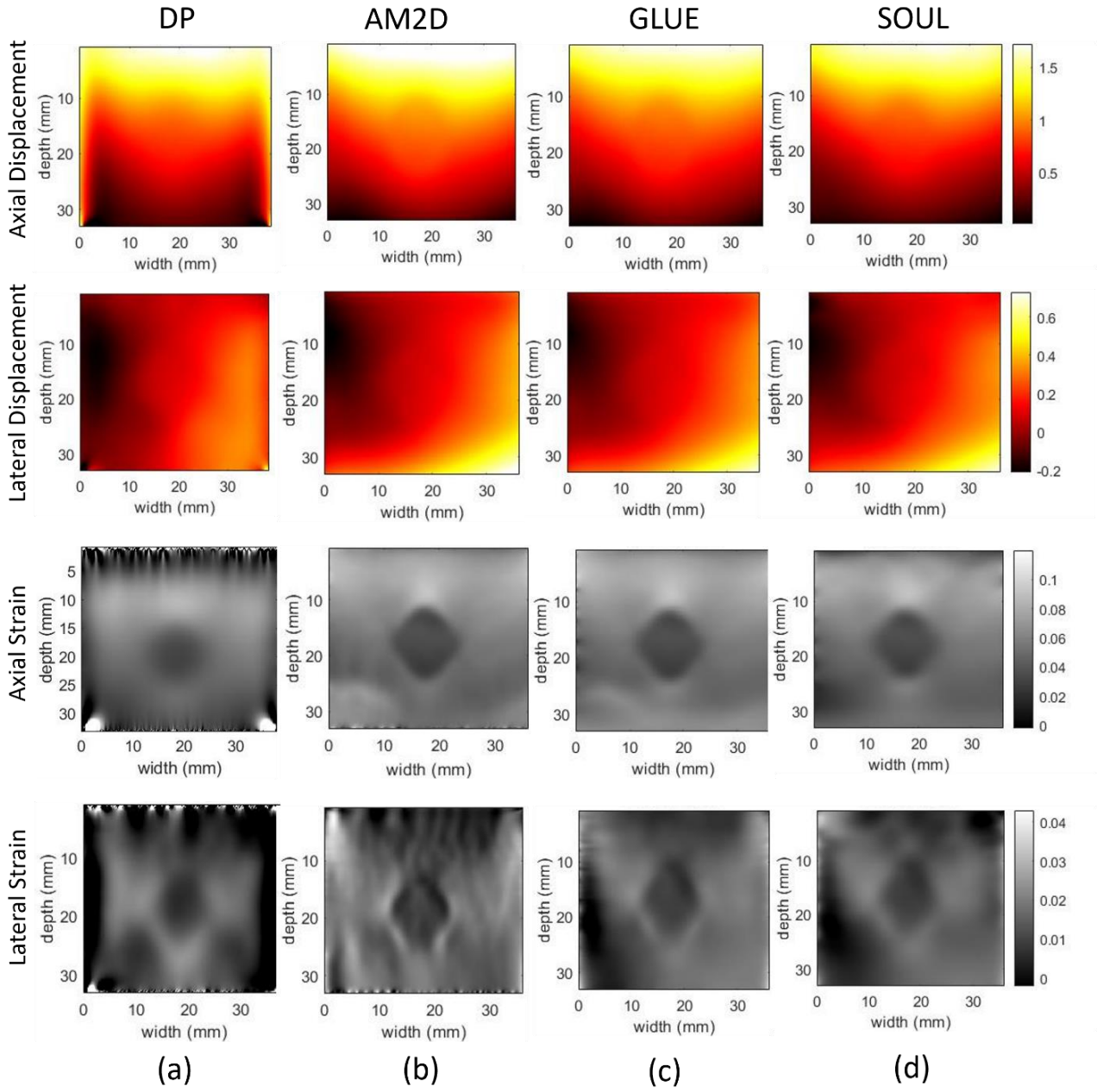

Figure 4-8. Displacement and strain images generated for the tissue-mimicking phantom case using different initial displacement estimates. Column (a), (b), (c) and (d) show the results obtained using the DP, AM2D, GLUE and SOUL methods to generate initial displacements, respectively.

The AM2D, GLUE, and SOUL methods were used to obtain initial displacement field estimates for the four clinical cases, with the results presented in Figures 4-9 to 4-12. In each figure, the top two rows show the axial and lateral displacements, while the bottom two rows show the axial and lateral strains. The displacement fields, obtained after the second step of STREAL, are relatively similar across the three methods. Displacement fields obtained through initial displacement estimates generated by the AM2D method are less refined than displacements obtained through initial estimates generated by the other methods. The quality of axial and lateral strain images is different for each patient case. The axial strain image of patient 1 generated through AM2D+STREAL method (Fig. 4-9 (a)) shows more consistency with the tumor outline that was delineated manually, whereas the lateral strain image produced by GLUE+STREAL in Fig. 4-9 (b) shows more consistency with the delineated tumor outline. For patient 2, as shown in Figure 4-10 (a), AM2D+STREAL produced a better image quality as it displays the tumor details with higher clarity compared to the other methods. The strain image results for patient 3 are shown in Figure 4-11 are close across all methods, with AM2D+STREAL showing slightly better axial strain image. Finally, AM2D+STRAL generated axial strain images that are more consistent with the tumor outline delineated manually for patient 4 (Figure 4-12 (a)) while GLUE+STREAL produced higher quality lateral strain images for this patient in as illustrated in Figure 4-12 (b).

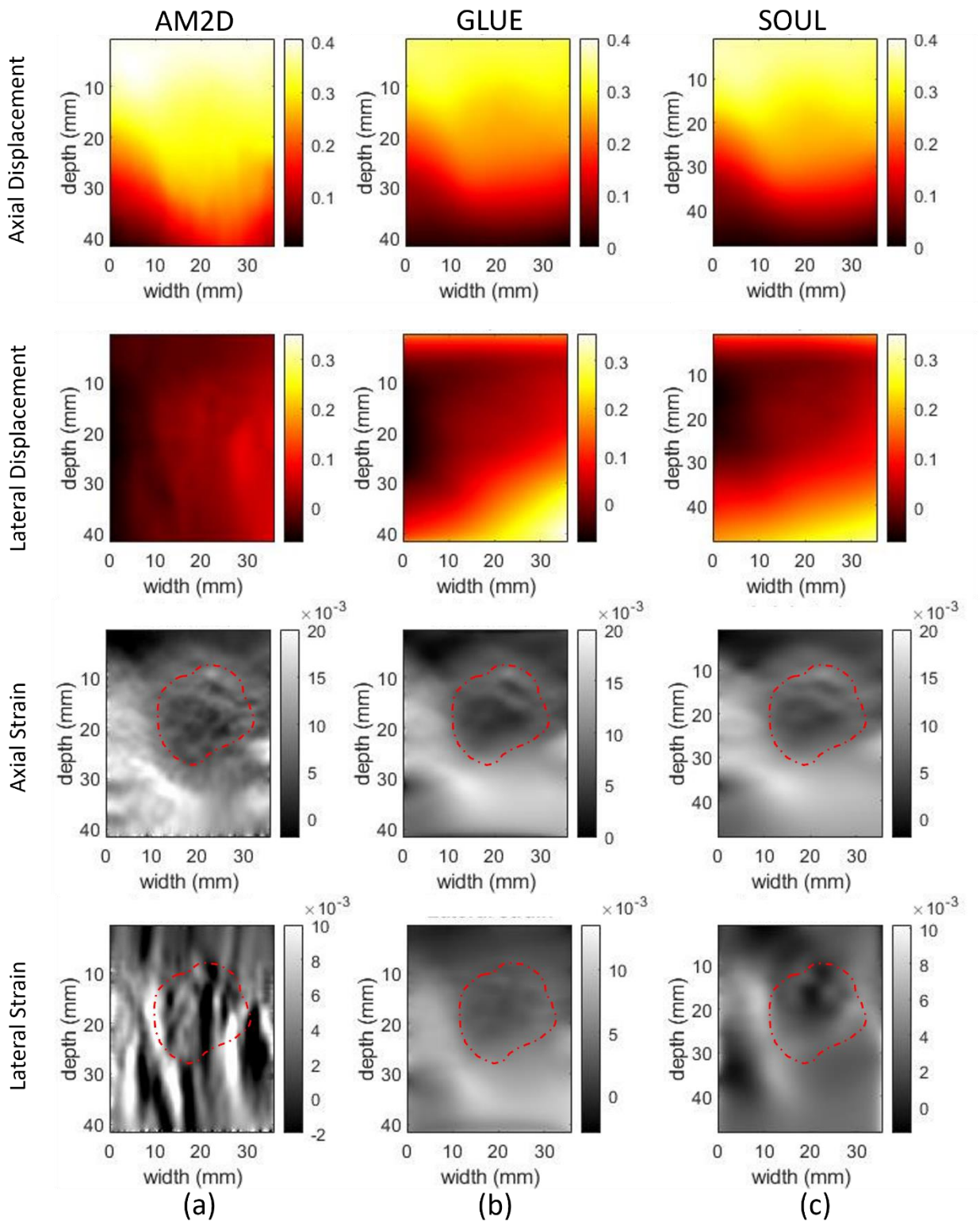

Figure 4-9. Displacement and strain images generated for patient 1 using the (a) AM2D, (b) GLUE, and (c) SOUL methods to obtain the initial displacement fields. The tumor region in each image is delineated with red dashed line.

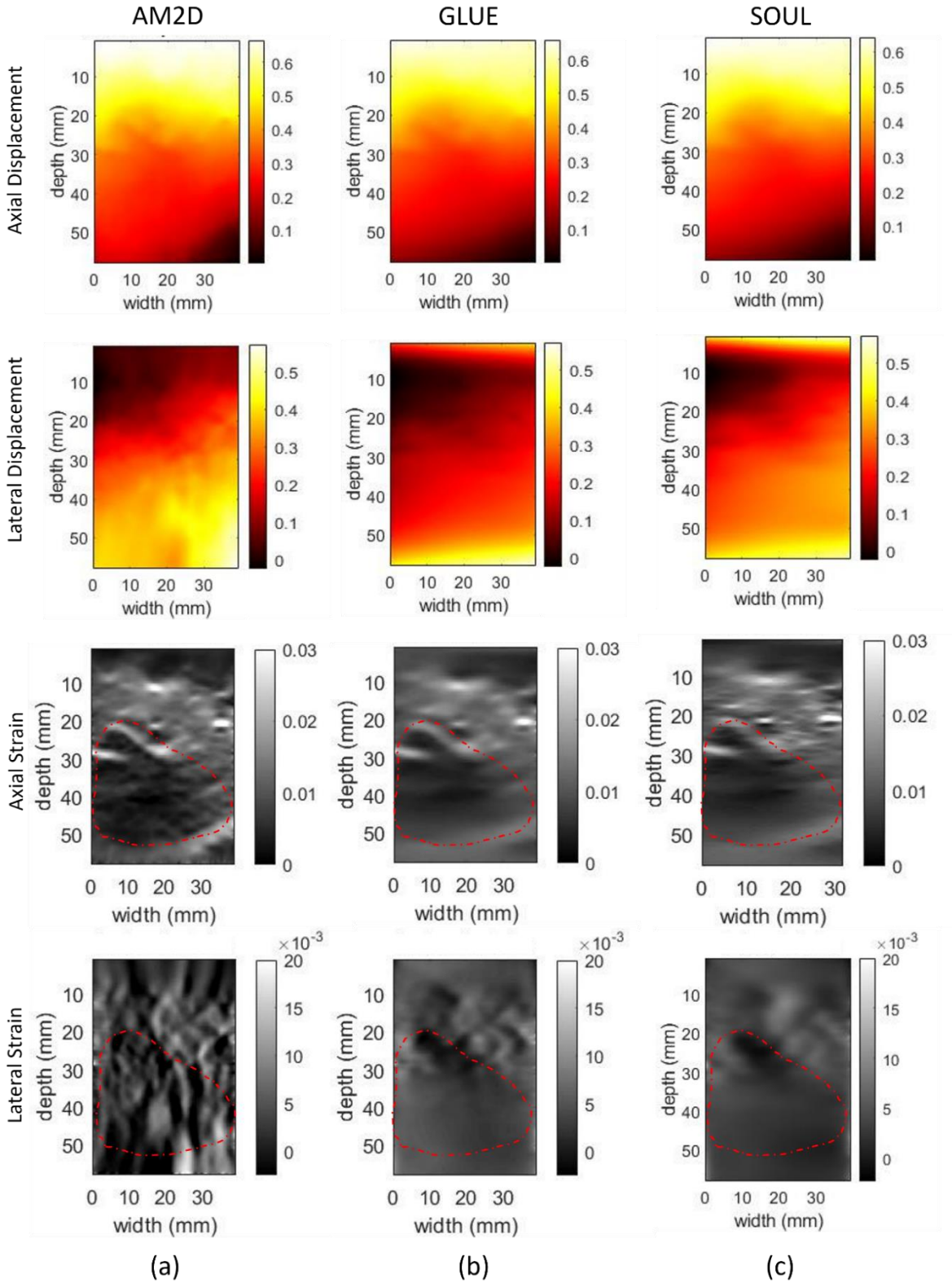

Figure 4-10. Displacement and strain images generated for patient 2 using the (a) AM2D, (b) GLUE, and (c) SOUL methods to obtain the initial displacement fields. The tumor region in each image is delineated with red dashed line.

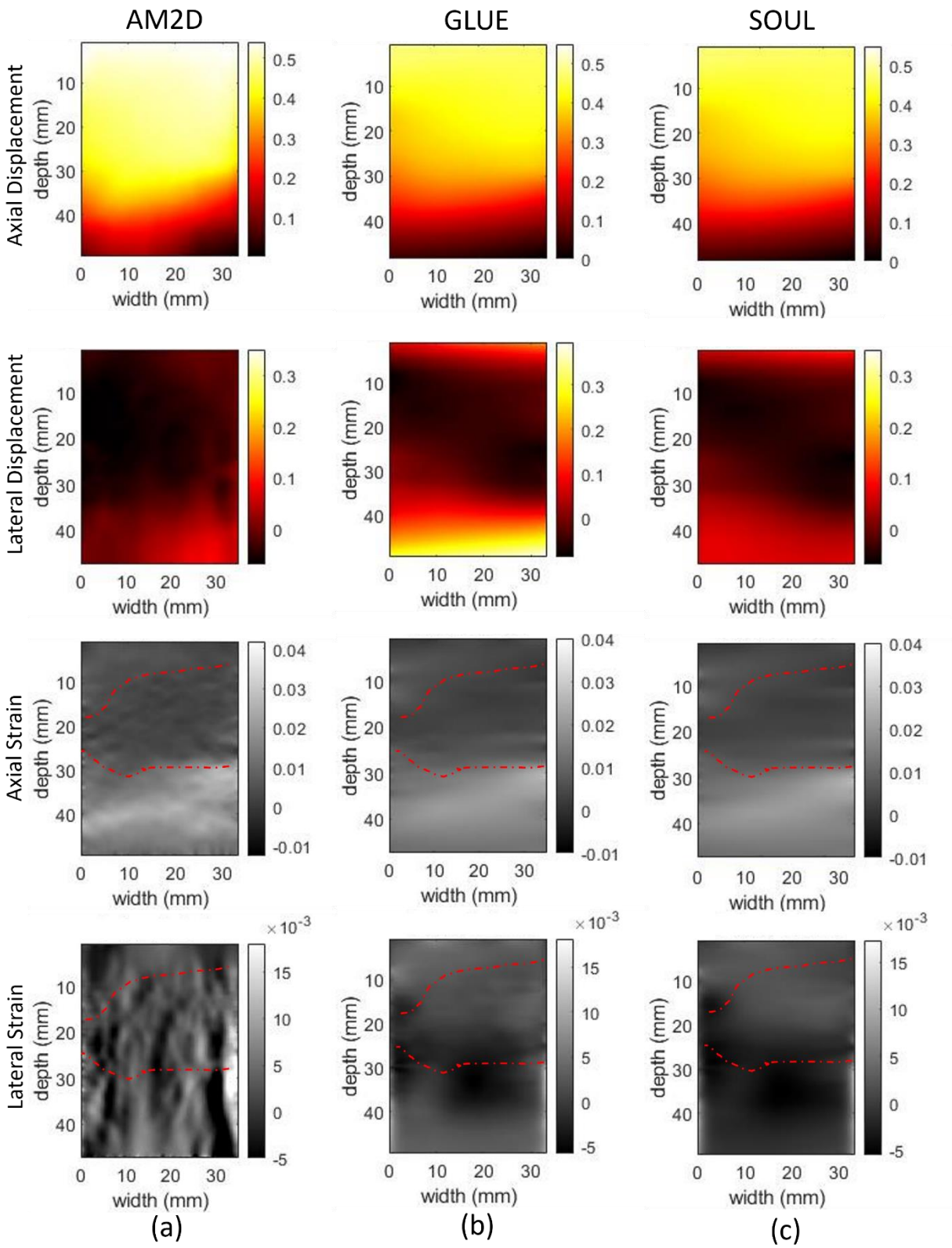

Figure 4-11. Displacement and strain images generated for patient 3 using the (a) AM2D, (b) GLUE, and (c) SOUL methods to obtain the initial displacement fields. The tumor region in each image is delineated with red dashed line.

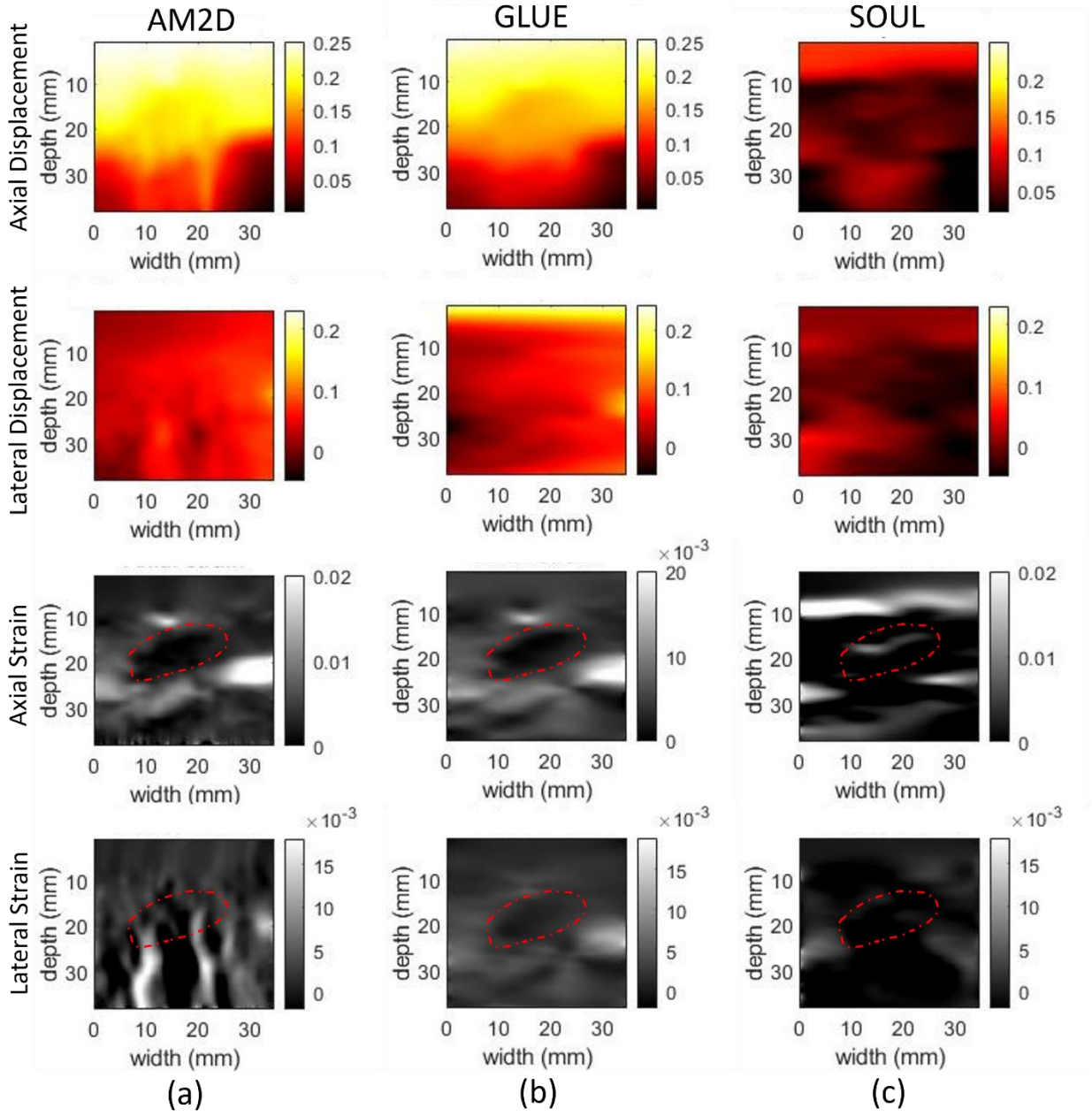

Figure 4-12. Displacement and strain images generated for patient 4 using the (a) AM2D, (b) GLUE, and (c) SOUL methods to obtain the initial displacement fields. The tumor region in each image is delineated with dashed line.

The tumor to background tissue stiffness ratio values calculated using the strain images are reported in Table 4-3. The tumor strain value applied for the stiffness ratio estimation was calculated as the average strain value within the tumor area which was segmented manually. The

strain value of the background tissue used for this estimation was calculated as the average strain value of the background area surrounding the tumor. As the phantom true stiffness ratio is known to be 1.70, the ratios obtained across the different methods show that the STREAL enhanced strain images produced closer ratio than the images produced by GLUE and SOUL only. Stiffness ratio values obtained from the axial and lateral strain images that are closest to the true value are bolded in the table for the phantom case. For the clinical cases where true values of stiffness ratio are unknown, the bolded values show the lowest difference between stiffness ratios obtained using the axial and lateral strain images, implying a better consistency between the lateral strain images with their axial strain counterparts in a preliminary quality assessment. For the phantom case, the stiffness ratio errors obtained through the axial strain images are 9.4%, 16.5%, 6.5%, 4.70%, and 4.70% for the GLUE, SOUL, GLUE+STREAL, SOUL+STREAL, and AM2D+STREAL methods, respectively. The stiffness ratio errors obtained using the lateral strain images are 28.23%, 35.29%, 10.58%, 26.47%, and 8.23% for the GLUE, SOUL, GLUE+STREAL, SOUL+STREAL, and AM2D+STREAL methods, respectively.

Table 4-3 Stiffness ratio in strain images obtained for the tissue-mimicking phantom and liver cancer patient cases. The values shown in bold font have the smallest stiffness ratio difference between axial and lateral strain images, and are the closest values to the ground-truth in the phantom case.

Method	**Phantom**		**Patient 1**		**Patient 2**		**Patient 3**		**Patient 4**	
	Axial Strain	*Lateral Strain*	*Axial Strain*	*Lateral Strain*	*Axial Strain*	*Lateral Strain*	*Axial Strain*	*Lateral Strain*	*Axial Strain*	*Lateral Strain*
GLUE	1.54	1.22	1.82	1.29	1.62	1.13	3.19	0.65	3.68	0.58
SOUL	1.42	1.10	1.65	1.42	1.60	1.37	3.21	5.11	4.82	0.71
GLUE+STREAL	1.81	1.52	**1.78**	**1.69**	1.63	1.07	**3.19**	**3.78**	4.21	2.50
SOUL+STREAL	1.78	1.25	1.83	1.60	**1.50**	**1.30**	2.73	1.31	**2.14**	**0.99**
AM2D+STREAL	**1.78**	**1.84**	1.66	2.11	1.96	1.70	4.01	1.11	3.78	1.188

4.2 *In silico* Liver Analysis

The simulated axial and lateral displacement fields in the FOV plane of the liver *in silico* models with different tumor sizes and locations under loading pertaining to three different US probe locations are illustrated in Figures 4-13, 4-14, and 4-15. In addition to the "ground truth" fields pertaining to the 3D liver model, simulated results pertaining to 2D approximate models of plane strain and plane stress are also illustrated. The displacement fields obtained from the 2D models show similar variations to the ground truth image in both axial and lateral directions. Table 4-4 shows calculated NMI values of the displacement fields obtained through the plane stress and plane strain models are compared to the ground truth displacements obtained from the 3D simulation. The highest NMI value at each position is highlighted. Generally, displacements obtained through plane stress models show higher NMI values, except for the axial displacement field obtained in position 2.

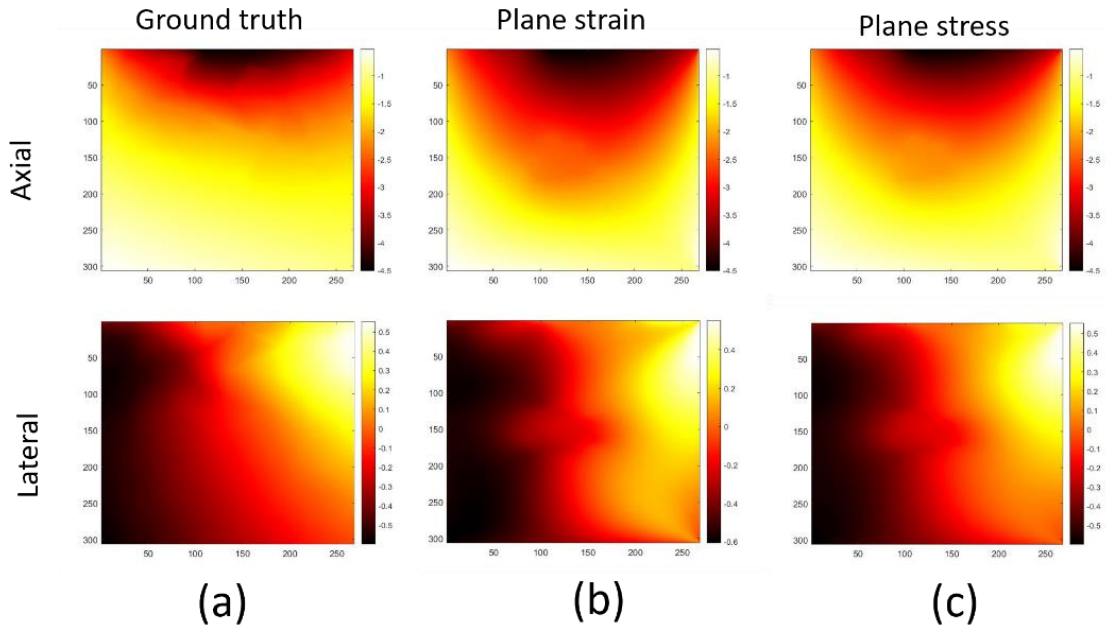

Figure 4-13. Displacement fields generated for US probe position 1 of the 3D *in silico* liver simulation (a), compared to the corresponding 2D plane strain model (b) and 2D plane stress model (c).

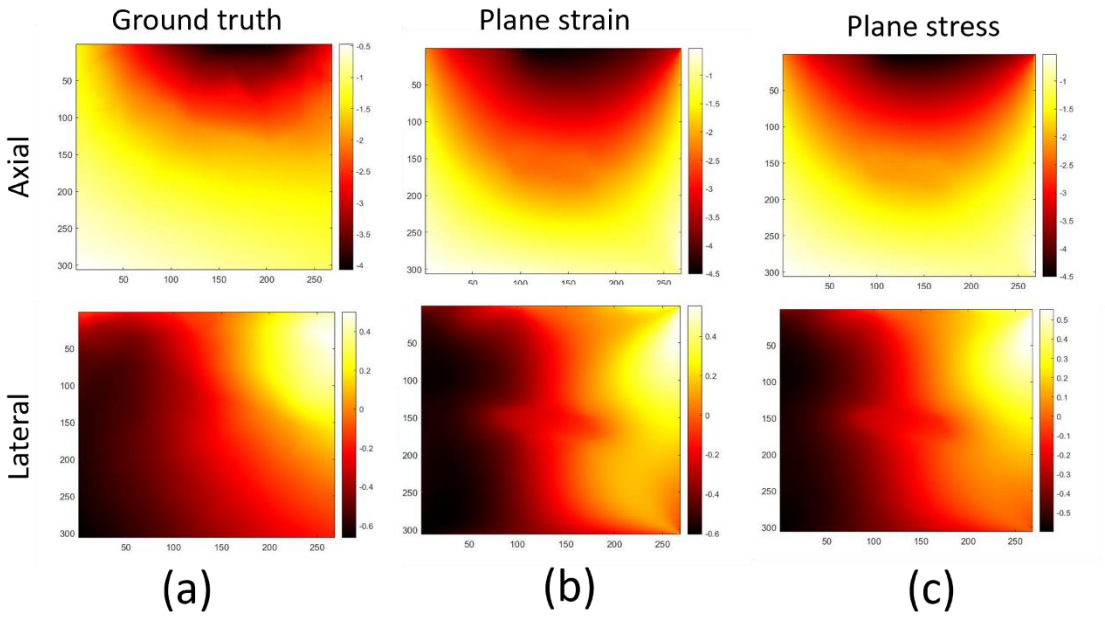

Figure 4-14. Displacement fields generated for US probe position 2 of the 3D *in silico* liver simulation (a), compared to the corresponding 2D plane strain model (b) and 2D plane stress model (c).

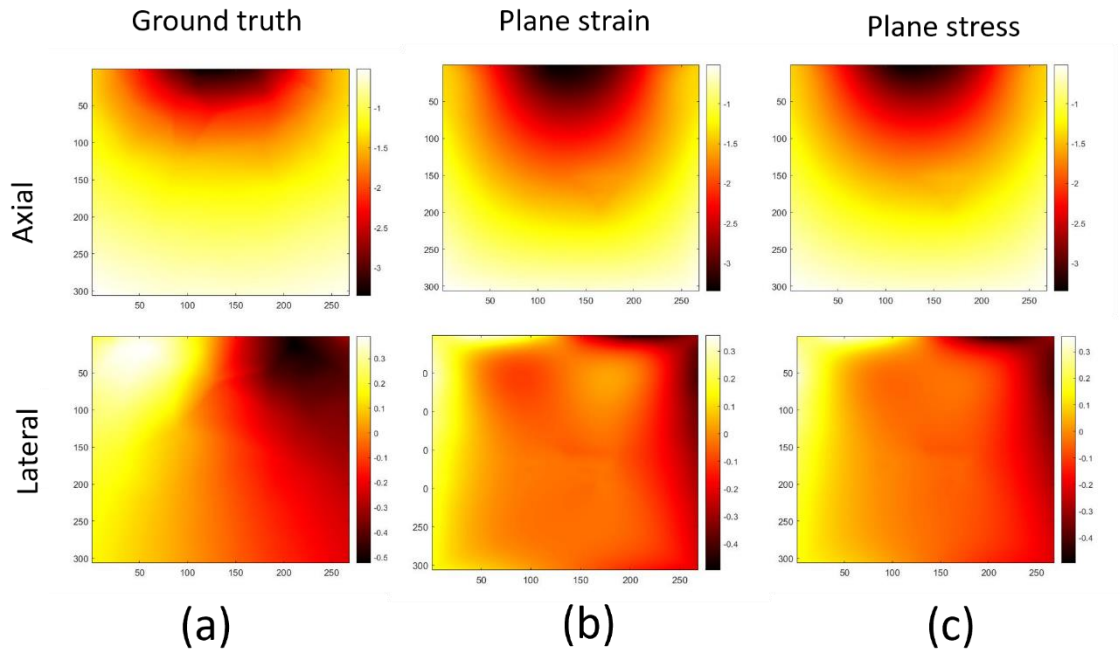

Figure 4-15. Displacement fields generated for US position 3 of the 3D *in silico* liver simulation (a), compared to the corresponding 2D plane strain model (b) and 2D plane stress model (c).

Table 4-4 NMI values obtained for comparing the displacement fields generated from the 2D plane stress and plane strain models to the fields obtained from the 3D liver model simulation.

Method	Position 1		Position 2		Position 2	
	Plane stress	*Plane strain*	*Plane stress*	*Plane strain*	*Plane stress*	*Plane strain*
Axial displacement	**1.0444**	1.0191	1.0297	**1.0324**	**1.1108**	1.0645
Lateral Displacement	**1.1086**	1.0293	**1.1000**	1.0330	**0.9895**	0.9492

4.3 Fulll-Inversion-Based Young's Modulus Reconstruction

Based on the results from the previous section, the plane stress assumption was used in the Young's modulus (E) recontruction as it was generally shown to lead to more realistic displacement fields, hence more realistic strain and stress fields than the plane strain model. The results obtained in the initial comparision between the original STREAL method (which utilizes initial displacement estimates produced by GLUE) and the GLUE and SOUL methods involved the E parameter reconstruction. In the reconstruction algorithm, the E reciprocal values obtained through axial and lateral strains were combined in each iteration using a weight ratio of 10:1, based on a similar noise amplitude ratio typically observed between the axial and lateral displacement data [62] Figures 4-16 and 4-17 show the reconstructed images of E obtaiend through displacements generated through the three methods. For the phantom case, the original STREAL method produced a Young's modulus image with a relatively better tumor to background contrast as shown in Figure 4-16. In the clinical cases, the contrast of tumor to background is more noticeable in the Young's modulus images associated with the original STREAL method for patients 1 and 3, while similar results were obtained using the three methods in case of patients 2 and 4. The inclusion to background stifness ratios estimated for the phantom case using the Young's modulus images associated with different methods have been presented in Table 4-5. As mentioned before, the true stiffness ratio of inclusion to the background in the phantom case is known to be 1.70. As shown in Table 4-5,

the Young's modulus reconstructed image using the original STREAL method achieved a ratio of 1.86, which corresponds to an error value of 9.4%. The Young's modulus image reconstructed using the GLUE method resulted in a ratio of 1.88, which corresponds to an error value of 10.58%. Using the SOUL method, a ratio of 1.86 was obtained which corresponds a similar value to STREAL of 9.4%.

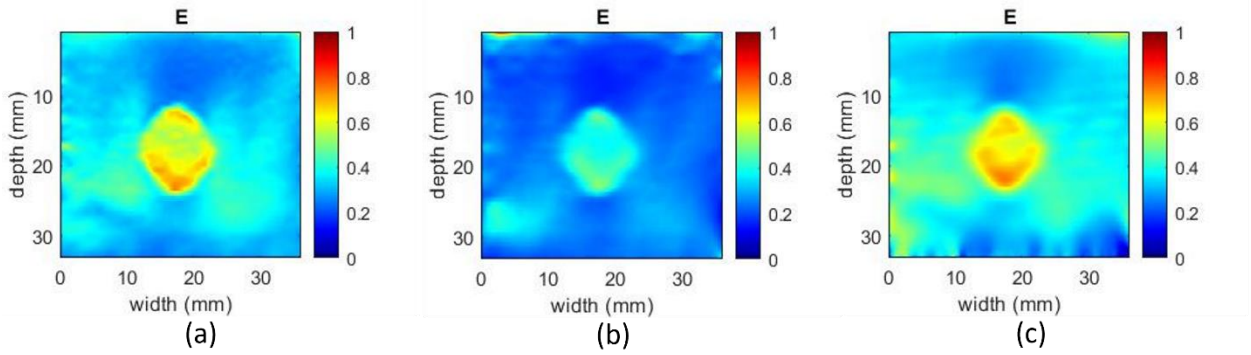

Figure 4-16 . Reconstructed Young's modulus images of the tissue mimicking phantom using (a) GLUE, (b) SOUL, and (c) STREAL.

Table 4-5 Inclusion to background stiffness ratio obtained from the reconstructed Young's modulus images.

Data	Method Used to Generate Strain Images					
	GLUE	**SOUL**	**DP+STREAL**	**GLUE+STREAL**	**SOUL+STREAL**	**AM2D+STREAL**
Phantom	1.88	1.86	1.48	1.86	1.87	**1.76**

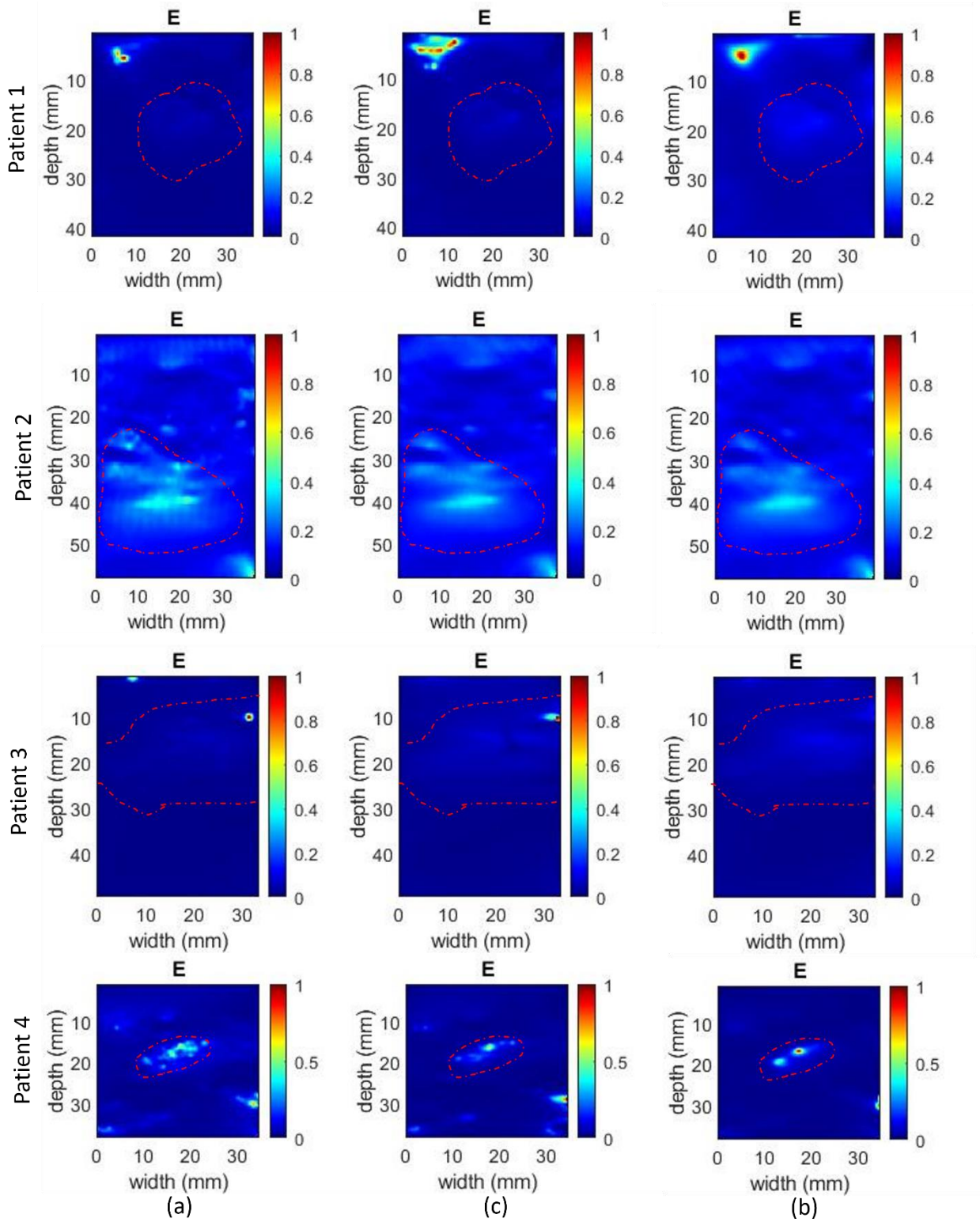

Figure 4-17 Reconstructed Young's modulus images for the clinical cases using (a) GLUE, (b) SOUL, and (c) STREAL. The tumor region in each image is delineated with red dashed line.

The axial and lateral strain images in Figures 4-8 to 4-12 generated using the STREAL method with the initial displacement field estimates obtained from different methods were applied to produce the Young's modulus images. For generating these images, the E reciprocal values obtained through axial and lateral strains in the reconstruction algorithm were combined in each iteration using a weight ratio of 10:1, as before. Figure 4-18 shows the reconstructed E image for the tissue mimicking phantom. Using the AM2D method to generate the displacement initial guess has shown a better image quality in terms of background and inclusion tissue homogeneity and higher consistency with the inclusion outline compared to the other methods as shown in Figure 4-18 (b). In Figure 4-18 (d), the extent of filtering is reduced to investigate the effect on the reconstructed E image. Figure 4-18 (d), where the SOUL method was used along with the STREAL method but without the first step of Laplacian filtering, shows less consistency with inclusion geometry compared to the image produced with using the Laplacian filtering step that is shown in Figure 4-18 (e). Table 4-5 illustrates the stiffness ratios obtained using the images in Figure 4-18. DP as initial estimate has resulted in the stiffness ratio with the highest error (10.58%), followed by SOUL with an error of 10%, GLUE having an error of 9.4%, and SOUL combined with STREAL without the Laplacian filtering with an error of 8.2%. Using AM2D to obtain the initial estimates has resulted in a stiffness ratio of 1.76 with the lowest error (3.5%), showing better result compared to both GLUE and SOUL alone, and all other initial estimation methods when combined with STREAL.

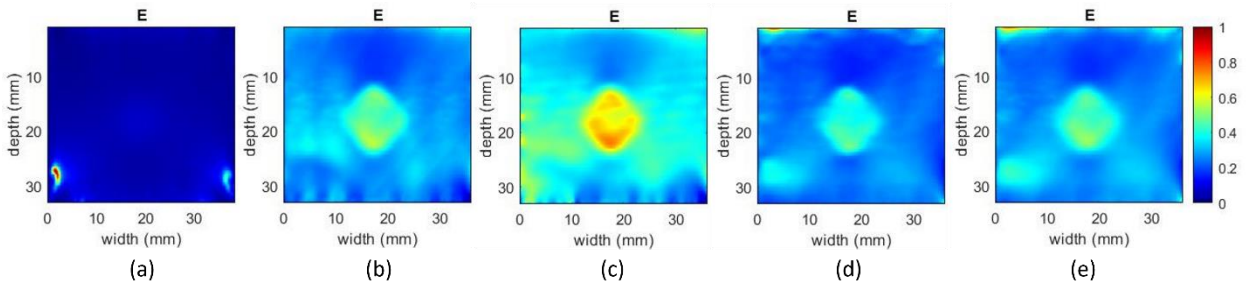

Figure 4-18. Reconstructed Young's modulus images of the tissue mimicking phantom using the STREAL method with initial displacement field estimates obtained from (a) DP, (b) AM2D, (c) GLUE, (d) SOUL+STREAL without Laplacian filtering, and (e) SOUL + full STREAL.

Figure 4-19 illustrates the E images for the clinical cases. The tumor regions are outlined with red dashed line. The results obtained using displacement initial estimates generated by the AM2D method generally show better contrast and more details of the tumor region compared to the images obtained using other initial guesses.

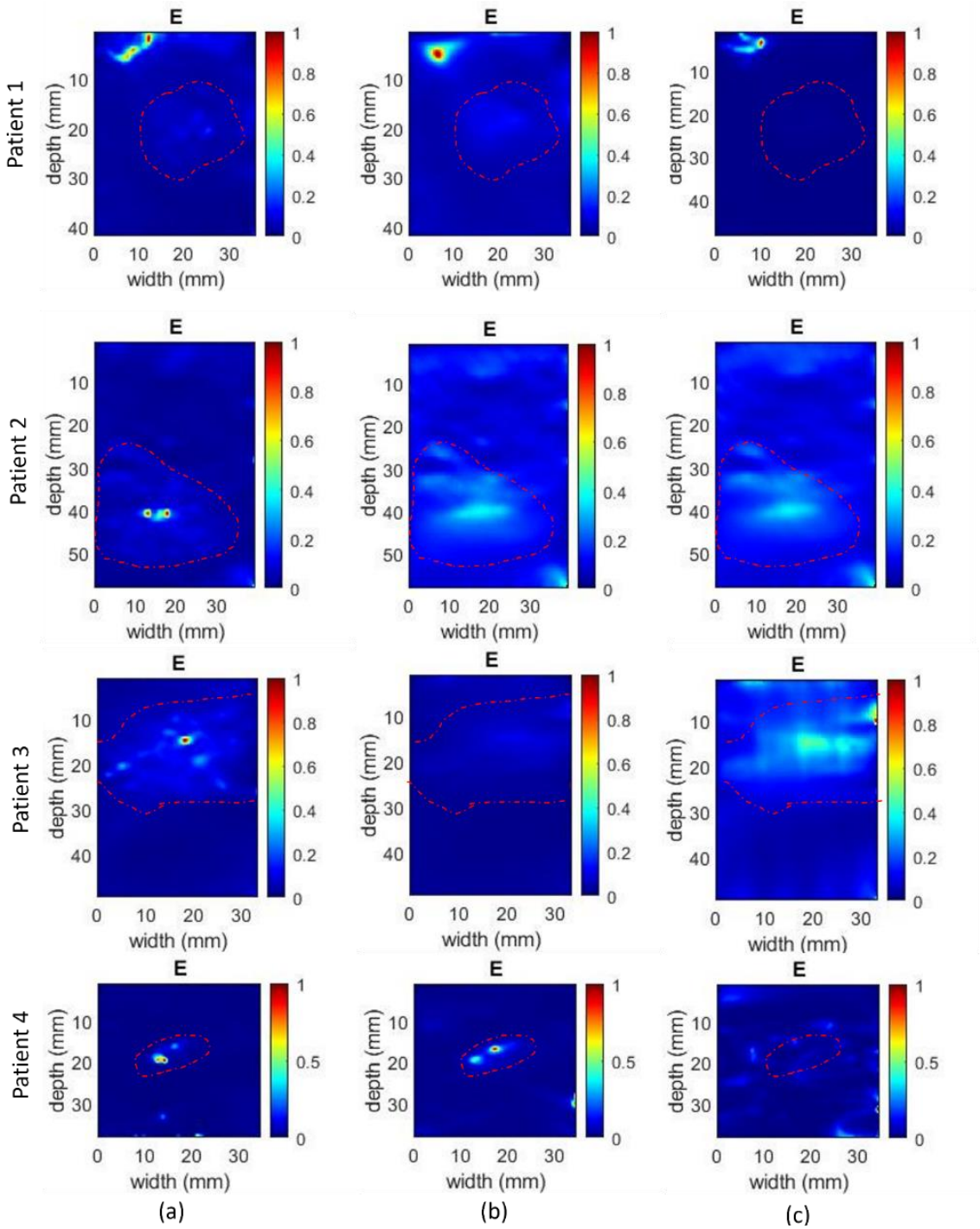

Figure 4-19. Reconstructed Young's modulus images for the clinical cases using the STREAL method with initial displacement estimates from (a) AM2D, (b) GLUE, and (c) SOUL. The tumor region in each image is delineated with red dashed line.

Chapter 5

Discussion and Conclusion

In this work, we investigated the application of a tissue mechanics-based strain refinement algorithm, along with a full-inversion-based elastic modulus reconstruction method for assessment of liver cancer. The strain refinement algorithm, STREAL, takes advantage of the tissue mechanics principles to enhance strain image accuracy. The tissue incompressibility principle is enforced by utilizing the Boussinesq semi-infinite analytical model to compensate for the out-of-plane strain component. Along with enforcing strain compatibility and displacement field continuity conditions, this method has shown to generate improved estimation of both axial and lateral displacement and strain images. Providing more accurate lateral displacement and strain images to be incorporated in elastic modulus reconstruction, the STREAL method can be utilized to effectively tackle the ill-posed inverse problem of the modulus reconstruction through using accurate estimate of lateral strain image in addition to the axial strain image. The STREAL method was adapted for liver elastography and was first investigated against other state of the art TDE methods in providing strain and E images, before investigating the use of different methods for providing the initial displacement estimate required for the STREAL method. An *in-silico* simulation was carried out to evaluate the performance of plane stress versus plane strain models in the 2D FE model approximation of the liver applied for full-inversion-based elasticity image reconstruction. The result was used as a basis to optimize the 2D FE model in the elastic modulus reconstruction method adapted for liver elastography [53], To our knowledge, no previous work has been carried out on full-inversion-based elastic modulus reconstruction in the liver. The methods were applied to a tissue mimicking phantom and four clinical cases pertaining to liver cancer patients who underwent ablation therapy.

5.1 Enhanced Strain Imaging

We compared the axial and lateral strain images obtained from the original STREAL method, which uses GLUE algorithm to obtain the initial displacement estimate, against other state of the art methods including the GLUE and SOUL. The GLUE method differs from previous window-based TDE techniques such as AM2D in that it estimates the displacement field of the entire image simultaneously to improve displacement continuity throughout the image [26]. The SOUL technique incorporates a second-order regularization term that has shown to lead to better strain image estimation compared to GLUE [40]. The quantitative results presented in Table 4-1 show the superiority of the STREAL method compared to the GLUE and SOUL methods in both the phantom and clinical studies in obtaining axial strain images. Furthermore, when comparing the standard deviation in the target and background windows in the axial and lateral strain images obtained for the tissue mimicking phantom, the STREAL method resulted in the lowest values, demonstrating a better consistency with the known homogeneity of the phantom's materials. Moreover, as the results in Table 4-3 demonstrate for the phantom, the STREAL method enhanced the strain images leading to the smallest error in stiffness ratio calculation for the phantom case, compared to those obtained using the GLUE and SOUL methods. Furthermore, compared to the STREAL method, the lateral strain images produced by the GLUE and SOUL methods demonstrate larger differences in stiffness ratio for the phantom and clinical cases, compared to their corresponding axial strain images. It is generally known that the latter images are more accurate.

The axial and lateral strain images generated using the STREAL method for both the tissue-mimicking phantom and clinical cases (Figures 4-3 to 4-7) usually show a better consistency with tumor/inclusion outline, with more refined strain images compared to those generated by the

GLUE and SOUL methods. The results show that the STREAL method improves on the GLUE method qualitatively and generally produces higher quality images compared to a state-of-the-art method known as SOUL, especially for lateral strain field. While existing motion tracking methods can produce relatively accurate axial strain images in tissue-mimicking phantoms, results obtained for clinical cases however are lower in quality, making them less reliable in the liver clinical applications. On the other hand, STREAL has shown higher quality lateral strain images in both the phantom and liver cancer patients, indicating its potential to be used effectively in a Young's modulus reconstruction algorithm, where both the axial and lateral strain image data are incorporated.

5.2 Accuracy/Robustness Assessment of STREAL with Various Initial Displacement Estimates

We further investigated the performance of the STREAL method and its robustness to the quality of the initial displacement estimates. Along with the original method that uses the GLUE algorithm for initial displacement estimation, we investigated the use of lower quality displacement estimates from the DP and AM2D methods as well as higher quality displacement estimates from the SOUL method as initial displacement estimates. The use of these methods was initially investigated on the tissue mimicking phantom as shown in Figure 4-8. While the resulting displacement images are relatively similar, the axial and lateral strain images produced by DP+STREAL have very low quality compared to the other methods. Meanwhile, as the stiffness ratio of the inclusion to background is known in the phantom, AM2D+STREAL has demonstrated the lowest error in both stiffness ratios estimated based on the axial and lateral strain images. This implies improved results over the original STREAL method which uses initial displacement estimated by the GLUE method.

The use of AM2D and SOUL as initial displacement estimators for STREAL, along with its original implementation, was investigated on four liver cancer patients (Figure 4-9 to 4-12). The AM2D+STREAL method showed a better axial strain image among the methods, with more details and better consistency with tumor outline delineated manually. However, it produced less refined lateral strain images in some cases, compared to the GLUE+STREAL method. The SOUL+STREAL method produced relatively similar results to the GLUE+STREAL method in both axial and lateral strain images in patient 2 and 3, with worse results in patient 1 and 4. The extent of smoothness in the initial results obtained from SOUL in clinical cases, which effects the results obtained from the SOUL+STREAL method could be attributed to the tunable parameters that could be further investigated and may affect the quality of lateral strain images. The over-smoothed axial strain images produced by SOUL+STREAL in some cases may be due to the higher noise suppression that is the result of the higher-order spatial continuity constraints used in SOUL, along with the Laplacian filtering applied in the first step of STREAL.

5.3 Full-inversion-based Elastography Using Strain Field Generated by STREAL

A full-inversion-based quasi-static US breast elastography method [53] was adapted for liver cancer assessment. Such assessment is performed based on the contrast in tissue stiffness that becomes apparent during cancer development process in solid tumors, compared to the surrounding normal tissue. This method has shown reliable E image reconstruction capabilities as it considers realistic boundary conditions in the reconstruction process, while accounting for stress non-uniformity within the tissue unlike strain imaging.

The displacement and strain images generated by the traditional TDE methods as well as the STREAL method with the proposed modifications were investigated as input to the full-inversion-

based Young's modulus reconstruction algorithm. We first compared the E image produced using the original STREAL, GLUE, and SOUL. Both the axial and lateral strain images were incorporated for the E image reconstruction with a higher weight assigned to the axial strain. For the phantom case, STREAL has shown to improve on the results by GLUE, as the stiffness ratio estimated using its associated E image demonstrated a lower error. However, SOUL resulted in a similar error compared to STREAL. The results obtained for the clinical cases have generally shown a clearer contrast between the tumor and background in the results produced by STREAL, compared to GLUE and SOUL.

We further investigated the use of STREAL with different initial displacement estimation to generate input images for the Young's modulus reconstruction algorithm. The reconstructed Young's modulus results of the tissue-mimicking phantom show that the lower quality strain image produced by DP+STREAL resulted in a low-quality E image with no clear inclusion outline. SOUL+STREAL without the Laplacian filtering in STREAL was also investigated to limit the excessive smoothing in the strain image. However, image (d) in Figure 4-18 shows less details about the inclusion geometry than image (e) where the full STREAL algorithm was used. The AM2D+STREAL method has produced the best results in the tissue mimicking phantom as shown in image (b) in Figure 4-18 where high consistency is visible with the inclusion geometry as well as a clearer difference in contrast between the tumor and the background. The proposed methods were further investigated on the liver cancer patients, using both axial and lateral strain images as input, where the AM2D+STREAL method has demonstrated consistent results in showing the tumor details and outline over the use of GLUE and SOUL as initial estimates. This indicates that using the AM2D method in conjunction with STREAL is not only sufficient but also superior for E image reconstruction. This may stem from the excessive smoothing involved when the GLUE

or SOUL methods are used, as a less smoothed strain image avoids excessive loss of signal which is enhanced through the STREAL process, leading to more reliable strain image input into the E image reconstruction.

5.4 Strengths and Limitations of the Proposed Method

5.4.1 Strengths

The use of STREAL method to obtain further refined displacement and strain images has shown to be effective based on both the tissue-mimicking phantom and liver cancer clinical cases. The observed improvements in the lateral strain component are more remarkable. This can be attributed to the fact that the incompressibility equation applied in the STREAL method incorporates a more accurate out-of-plane strain estimation using the Boussinesq's model while the compatibility equation constraint ensures strains consistent with displacement continuity that may be lost through the computational process.

Our result not only showed the good performance of the original STREAL implementation on liver clinical applications over other state of the art methods but also showed that the STREAL method is relatively robust to the quality of the initial displacement estimates and can generate accurate axial and lateral strain images in clinical applications using lower quality initial displacement fields estimated by less-advanced methods such as AM2D. While the SOUL method has also shown to generate relatively accurate axial strain image results, STREAL has outperformed SOUL in generating high-quality lateral strain images. The results demonstrate the strength of using STREAL to obtain high quality axial and lateral strain images over other methods

The adapted Young's modulus reconstruction method has outperformed the strain imaging methods in showing tumor outlines and detail, and it can provide more accurate estimation of

tumor to background tissue stiffness ratio. Tissue stiffness ratio is the major source of contrast in elastography images and can serve as a quantitative biomarker for lesion detection during liver ablation surgeries. The use of both lateral and axial strain images in the reconstruction can aid in improving the reconstructed E image by providing extra details that the axial strain image alone may not provide.

All in all, the proposed method can be easily implemented into conventional US machines, as it does not require extra hardware elements with respect to mechanical stimulation. The strain refinement algorithm and the E image reconstruction method only requires US RF frames acquired at pre- and post-compression states as the measured input, making it easy to adapt in clinical applications.

5.4.2 Limitations of the Method

The proposed method when used with a higher quality initial displacement estimate such as SOUL, typically leads to overrefined strain images losing important details about the tumor boundaries. One of the potential limitations of the proposed method is that its implementation may not be straightforward for real-time US applications, due to the longer computational time associated with it compared to conventional strain imaging. However, this can be addressed through a GPU programming approach such as the one applied in [63]. The reconstruction process can involve errors because of inaccuracies in the estimated axial and lateral boundary conditions. Another source of error in the reconstruction process is inaccurate stress field estimation in the 2D FE model which approximate an ideal 3D FE model with patient-specific liver geometry. This error can be reduced to an extent using a 2D plane stress (rather than plane strain) model, chosen based on the results obtained from the conducted *in silico* simulations. The conclusions of this project are based on preliminary results obtained through a tissue-mimicking phantom study and a pilot

clinical study with limited sample size. More concrete conclusions can be made upon completing extended phantom and clinical studies with rigorous statistical evaluations.

5.5 Future Directions

While the proposed method has shown promising results in a small pilot clinical study for liver cancer assessment, further investigation on a larger clinical study including different lesion types is required to assess its performance rigorously in clinical settings. The method has the potential for detecting and characterizing liver tumors during ablation therapies using the generated elastography images and estimated tissue stiffness ratios, and for monitoring the outcome of the treatment using the quantitative data acquired before and after ablation.

Recently, the field of machine learning has been growing rapidly. Therefore, it is worth investigating the use of data-driven deep-learning-based methods such as the one proposed in [39] to estimate initial displacement fields for the STREAL method. Furthermore, as the original STREAL method was designed for the breast, the improved STREAL method introduced in this work for liver elastography can be extended to and explored for other organs.

References

[1] "The top 10 causes of death." https://www.who.int/news-room/fact-sheets/detail/the-top-10-causes-of-death (accessed May 22, 2022).

[2] "What Is Cancer? - NCI." https://www.cancer.gov/about-cancer/understanding/what-is-cancer (accessed May 22, 2022).

[3] "What Is Liver Cancer?" https://www.cancer.org/cancer/liver-cancer/about/what-is-liver-cancer.html (accessed May 23, 2022).

[4] "Liver: Anatomy and Functions | Johns Hopkins Medicine." https://www.hopkinsmedicine.org/health/conditions-and-diseases/liver-anatomy-and-functions (accessed May 22, 2022).

[5] P. N. Span, J. Humphries, M. Zegers, S. S. Deville, and N. Cordes, "The Extracellular, Cellular, and Nuclear Stiffness, a Trinity in the Cancer Resistome-A Review," *Frontiers in Oncology | www.frontiersin.org*, vol. 9, p. 1376, 2019, doi: 10.3389/fonc.2019.01376.

[6] "Liver (Anatomy): Picture, Function, Conditions, Tests, Treatments." https://www.webmd.com/digestive-disorders/picture-of-the-liver (accessed May 22, 2022).

[7] R. G. Barr, "Elastography in Clinical Practice," *Radiologic Clinics of North America*, vol. 52, no. 6, pp. 1145–1162, Nov. 2014, doi: 10.1016/J.RCL.2014.07.002.

[8] "Liver Cancer: Statistics | Cancer.Net." https://www.cancer.net/cancer-types/liver-cancer/statistics (accessed May 14, 2022).

[9] "Liver cancer - Symptoms and causes - Mayo Clinic." https://www.mayoclinic.org/diseases-conditions/liver-cancer/symptoms-causes/syc-20353659 (accessed May 23, 2022).

[10] B. Zavan, F. Barbieri, E. Rovida, D. Gurbani, M. Kalli, and T. Stylianopoulos, "Defining the Role of Solid Stress and Matrix Stiffness in Cancer Cell Proliferation and Metastasis," *Front. Oncol*, vol. 8, p. 55, 2018, doi: 10.3389/fonc.2018.00055.

[11] H. Sung *et al.*, "Global Cancer Statistics 2020: GLOBOCAN Estimates of Incidence and Mortality Worldwide for 36 Cancers in 185 Countries," *CA: A Cancer Journal for Clinicians*, vol. 71, no. 3, pp. 209–249, May 2021, doi: 10.3322/CAAC.21660.

[12] PDQ Adult Treatment Editorial Board, "Adult Primary Liver Cancer Treatment (PDQ®): Health Professional Version," *PDQ Cancer Information Summaries*, 2002, Accessed: May 15, 2022. [Online]. Available: http://www.ncbi.nlm.nih.gov/pubmed/26389465

[13] M. R. Oliva and S. Saini, "Liver cancer imaging: Role of CT, MRI, US and PET," *Cancer Imaging*, vol. 4, 2004, doi: 10.1102/1470-7330.2004.0011.

[14] "Magnetic Resonance Imaging (MRI)." https://www.nibib.nih.gov/science-education/science-topics/magnetic-resonance-imaging-mri (accessed May 16, 2022).

[15] K. M. Hasebroock and N. J. Serkova, "Toxicity of MRI and CT contrast agents," *Expert Opinion on Drug Metabolism & Toxicology*, vol. 5, no. 4, pp. 403–416, 2009, doi: 10.1517/17425250902873796.

[16] "Positron emission tomography (PET) scan | Canadian Cancer Society." https://cancer.ca/en/treatments/tests-and-procedures/positron-emission-tomography-pet-scan (accessed May 16, 2022).

[17] J. L. Gennisson, T. Deffieux, M. Fink, and M. Tanter, "Ultrasound elastography: Principles and techniques," *Diagnostic and Interventional Imaging*, vol. 94, no. 5, pp. 487–495, May 2013, doi: 10.1016/J.DIII.2013.01.022.

[18] W. C. Yeh *et al.*, "Elastic modulus measurements of human liver and correlation with pathology," *Ultrasound in Medicine and Biology*, vol. 28, no. 4, pp. 467–474, 2002, doi: 10.1016/S0301-5629(02)00489-1.

[19] V. Chernyak *et al.*, "Liver Imaging Reporting and Data System (LI-RADS) Version 2018: Imaging of Hepatocellular Carcinoma in At-Risk Patients," *Radiology*, vol. 289, no. 3, pp. 816–830, Dec. 2018, doi: 10.1148/RADIOL.2018181494.

[20] K. Kato, H. Sugimoto, N. Kanazumi, S. Nomoto, S. Takeda, and A. Nakao, "Intra-operative application of real-time tissue elastography for the diagnosis of liver tumours", doi: 10.1111/j.1478-3231.2008.01701.x.

[21] T. J. Vogl, M. P. Dosch, and Y. Haas, "MR elastography is a good response parameter for microwave ablation liver tumors," *European Journal of Radiology*, vol. 152, p. 110360, Jul. 2022, doi: 10.1016/J.EJRAD.2022.110360.

[22] T. Varghese, J. A. Zagzebski, and F. T. Lee, "Elastographic imaging of thermal lesions in the liver in vivo following radiofrequency ablation: Preliminary results," *Ultrasound in Medicine and Biology*, vol. 28, no. 11–12, pp. 1467–1473, Nov. 2002, doi: 10.1016/S0301-5629(02)00656-7.

[23] J. Ophir, I. Céspedes, H. Ponnekanti, Y. Yazdi, and X. li, "Elastography: A quantitative method for imaging the elasticity of biological tissues," *Ultrasonic Imaging*, vol. 13, no. 2, pp. 111–134, Aug. 1991, doi: 10.1177/016173469101300201.

[24] A. Samani, J. Bishop, and D. B. Plewes, "A constrained modulus reconstruction technique for breast cancer assessment," *IEEE Trans Med Imaging*, vol. 20, no. 9, pp. 877–885, Sep. 2001, doi: 10.1109/42.952726.

[25] H. Rivaz, E. M. Boctor, M. A. Choti, and G. D. Hager, "Real-time regularized ultrasound elastography," *IEEE Trans Med Imaging*, vol. 30, no. 4, pp. 928–945, Apr. 2011, doi: 10.1109/TMI.2010.2091966.

[26] H. S. Hashemi and H. Rivaz, "Global Time-Delay Estimation in Ultrasound Elastography," *IEEE Trans Ultrason Ferroelectr Freq Control*, vol. 64, no. 10, pp. 1625–1636, Oct. 2017, doi: 10.1109/TUFFC.2017.2717933.

[27] R. M. S. Sigrist, J. Liau, A. el Kaffas, M. C. Chammas, and J. K. Willmann, "Ultrasound Elastography: Review of Techniques and Clinical Applications," *Theranostics*, vol. 7, no. 5, pp. 1303–1329, 2017, doi: 10.7150/THNO.18650.

[28] H. Yu and S. R. Wilson, "Differentiation of benign from malignant liver masses with Acoustic Radiation Force Impulse technique," *Ultrasound Q*, vol. 27, no. 4, pp. 217–223, Dec. 2011, doi: 10.1097/RUQ.0B013E318239422E.

[29] M. Xuelei *et al.*, “Elastography for the differentiation of benign and malignant liver lesions: a meta-analysis,” *Tumour Biol*, vol. 35, no. 5, pp. 4489–4497, 2014, doi: 10.1007/S13277-013-1591-4.

[30] C. Goya *et al.*, “The Role of Acoustic Radiation Force Impulse Elastography in the Differentiation of Infectious and Neoplastic Liver Lesions,” *Ultrason Imaging*, vol. 37, no. 4, pp. 312–322, Oct. 2015, doi: 10.1177/0161734614566697.

[31] L. Sandrin *et al.*, “Transient elastography: a new noninvasive method for assessment of hepatic fibrosis,” *Ultrasound Med Biol*, vol. 29, no. 12, pp. 1705–1713, 2003, doi: 10.1016/J.ULTRASMEDBIO.2003.07.001.

[32] L. Castera, X. Forns, and A. Alberti, “Non-invasive evaluation of liver fibrosis using transient elastography,” *J Hepatol*, vol. 48, no. 5, pp. 835–847, May 2008, doi: 10.1016/J.JHEP.2008.02.008.

[33] S. K. Venkatesh *et al.*, “MR elastography of liver tumors: Preliminary results,” *American Journal of Roentgenology*, vol. 190, no. 6, pp. 1534–1540, Jun. 2008, doi: 10.2214/AJR.07.3123.

[34] S. R. Ara *et al.*, “Phase-based direct average strain estimation for elastography,” *IEEE Trans Ultrason Ferroelectr Freq Control*, vol. 60, no. 11, pp. 2266–2283, 2013, doi: 10.1109/TUFFC.2013.6644732.

[35] Y. Wang, M. Bayer, J. Jiang, and T. J. Hall, “An Improved Region-Growing Motion Tracking Method Using More Prior Information for 3-D Ultrasound Elastography,” *IEEE Trans Ultrason Ferroelectr Freq Control*, vol. 67, no. 3, pp. 580–597, Mar. 2020, doi: 10.1109/TUFFC.2019.2948984.

[36] M. Mirzaei, A. Asif, M. Fortin, and H. Rivaz, “3D normalized cross-correlation for estimation of the displacement field in ultrasound elastography,” *Ultrasonics*, vol. 102, p. 106053, Mar. 2020, doi: 10.1016/J.ULTRAS.2019.106053.

[37] L. Yuan and P. C. Pedersen, “Analytical phase-tracking-based strain estimation for ultrasound elasticity,” *IEEE Transactions on Ultrasonics, Ferroelectrics, and Frequency Control*, vol. 62, no. 1, pp. 185–207, Jan. 2015, doi: 10.1109/TUFFC.2014.006701.

[38] X. Pan, J. Gao, S. Tao, K. Liu, J. Bai, and J. Luo, “A two-step optical flow method for strain estimation in elastography: Simulation and phantom study,” *Ultrasonics*, vol. 54, no. 4, pp. 990–996, Apr. 2014, doi: 10.1016/J.ULTRAS.2013.11.010.

[39] Md. G. Kibria and H. Rivaz, “Global Ultrasound Elastography Using Convolutional Neural Network,” *Lecture Notes in Computer Science (including subseries Lecture Notes in Artificial Intelligence and Lecture Notes in Bioinformatics)*, vol. 11042 LNCS, pp. 21–28, May 2018, doi: 10.1007/978-3-030-01045-4_3.

[40] M. Ashikuzzaman, A. Sadeghi-Naini, A. Samani, and H. Rivaz, “Combining First- And Second-Order Continuity Constraints in Ultrasound Elastography,” *IEEE Transactions on Ultrasonics, Ferroelectrics, and Frequency Control*, vol. 68, no. 7, pp. 2407–2418, Jul. 2021, doi: 10.1109/TUFFC.2021.3065884.

[41] M. A. Lubinski, "Lateral displacement estimation using tissue incompressibility," *IEEE Transactions on Ultrasonics, Ferroelectrics, and Frequency Control*, vol. 43, no. 2, pp. 247–256, 1996, doi: 10.1109/58.485950.

[42] N. Kheirkhah, S. C. H. Dempsey, H. Rivaz, A. Samani, and A. Sadeghi-Naini, "A Tissue Mechanics Based Method to Improve Tissue Displacement Estimation in Ultrasound Elastography," *Proceedings of the Annual International Conference of the IEEE Engineering in Medicine and Biology Society, EMBS*, vol. 2020-July, pp. 2051–2054, Jul. 2020, doi: 10.1109/EMBC44109.2020.9175869.

[43] H. Rivaz, E. M. Boctor, M. A. Choti, and G. D. Hager, "Ultrasound elastography using multiple images," *Medical Image Analysis*, vol. 18, no. 2, pp. 314–329, Feb. 2014, doi: 10.1016/J.MEDIA.2013.11.002.

[44] A. R. Skovoroda, M. A. Lubinski, S. Y. Emelianov, and M. O'Donnell, "Nonlinear estimation of the lateral displacement using tissue incompressibility," *IEEE Transactions on Ultrasonics, Ferroelectrics, and Frequency Control*, vol. 45, no. 2, pp. 491–503, 1998, doi: 10.1109/58.660158.

[45] H. Li, J. Porée, B. Chayer, M. H. R. Cardinal, and G. Cloutier, "Parameterized Strain Estimation for Vascular Ultrasound Elastography with Sparse Representation," *IEEE Transactions on Medical Imaging*, vol. 39, no. 12, pp. 3788–3800, Dec. 2020, doi: 10.1109/TMI.2020.3005017.

[46] D. T. Seidl, A. A. Oberai, and P. E. Barbone, "The Coupled Adjoint-State Equation in forward and inverse linear elasticity: Incompressible plane stress," *Computer Methods in Applied Mechanics and Engineering*, vol. 357, p. 112588, Dec. 2019, doi: 10.1016/J.CMA.2019.112588.

[47] A. L. Duroy, V. Detti, A. Coulon, O. Basset, and E. Brusseau, "2D tissue strain tensor imaging in quasi-static ultrasound elastography," *Proceedings of the Annual International Conference of the IEEE Engineering in Medicine and Biology Society, EMBS*, pp. 2847–2851, 2021, doi: 10.1109/EMBC46164.2021.9630570.

[48] K. R. Raghavan and A. E. Yagle, "Forward and Inverse Problems in Elasticity Imaging of Soft Tissues," *IEEE Transactions on Nuclear Science*, vol. 41, no. 4, pp. 1639–1648, 1994, doi: 10.1109/23.322961.

[49] F. Kallel and M. Bertrand, "Tissue elasticity reconstruction using linear perturbation method," *IEEE Transactions on Medical Imaging*, vol. 15, no. 3, pp. 299–313, 1996, doi: 10.1109/42.500139.

[50] A. A. Oberai, N. H. Gokhale, and G. R. Feijóo, "Solution of inverse problems in elasticity imaging using the adjoint method," *Inverse Problems*, vol. 19, no. 2, p. 297, Feb. 2003, doi: 10.1088/0266-5611/19/2/304.

[51] M. M. Doyley, J. C. Bamber, T. Shiina, and M. O. Leach, "Reconstruction of elastic modulus distribution from envelope detected B-mode data," *1996 IEEE Ultrasonics Symposium. Proceedings*, vol. 2, pp. 1611–1614, doi: 10.1109/ULTSYM.1996.584397.

[52] A. Samani, J. Bishop, and D. B. Plewes, "A constrained modulus reconstruction technique for breast cancer assessment," *IEEE Transactions on Medical Imaging*, vol. 20, no. 9, pp. 877–885, Sep. 2001, doi: 10.1109/42.952726.

[53] S. R. Mousavi, H. Rivaz, A. Sadeghi-Naini, G. J. Czarnota, and A. Samani, “Breast Ultrasound Elastography Using Full Inversion-Based Elastic Modulus Reconstruction,” *IEEE Transactions on Computational Imaging*, vol. 3, no. 4, 2017, doi: 10.1109/tci.2017.2741422.

[54] W. Scholarship, N. Kheirkhah, and J. Supervisor, “A Novel Ultrasound Elastography Technique for Evaluating Tumor A Novel Ultrasound Elastography Technique for Evaluating Tumor Response to Neoadjuvant Chemotherapy in Patients with Locally Response to Neoadjuvant Chemotherapy in Patients with Locally Advanced Breast Cancer Advanced Breast Cancer,” 2022.

[55] A. Tikhonov, “Solution of Incorrectly Formulated Problems and the Regularization Method,” 1963.

[56] E. Polak and G. Ribiere, “REVUE FRANÇAISE D’INFORMATIQUE ET DE RECHERCHE OPÉRATIONNELLE. SÉRIE ROUGE Note sur la convergence de méthodes de directions conjuguées”, Accessed: Jun. 21, 2022. [Online]. Available: http://www.numdam.org/conditions

[57] B. J. , K. S. , L. Y. , B. O. , K. M. , G. C. , … L. J. , P. S. M. D. P. M. T. L. P. F. Erickson, “Radiology Data from The Cancer Genome Atlas Liver Hepatocellular Carcinoma [TCGA-LIHC] collection. The Cancer Imaging Archive.” 2016. doi: http://doi.org/10.7937/K9/TCIA.2016.IMMQW8UQ.

[58] K. Clark *et al.*, “The Cancer Imaging Archive (TCIA): maintaining and operating a public information repository,” *J Digit Imaging*, vol. 26, no. 6, pp. 1045–1057, Dec. 2013, doi: 10.1007/S10278-013-9622-7.

[59] “3D Slicer image computing platform | 3D Slicer.” https://www.slicer.org/ (accessed May 29, 2022).

[60] A. Fedorov *et al.*, “3D Slicer as an Image Computing Platform for the Quantitative Imaging Network,” *Magn Reson Imaging*, vol. 30, no. 9, pp. 1323–1341, 2012, doi: 10.1016/j.mri.2012.05.001.

[61] H. Rivaz, E. M. Boctor, M. A. Choti, and G. D. Hager, “Real-time regularized ultrasound elastography,” *IEEE Trans Med Imaging*, vol. 30, no. 4, pp. 928–945, Apr. 2011, doi: 10.1109/TMI.2010.2091966.

[62] T. L. Szabo, “Diagnostic Ultrasound Imaging: Inside Out: Second Edition,” *Diagnostic Ultrasound Imaging: Inside Out: Second Edition*, pp. 1–549, 2004, doi: 10.1016/C2011-0-07261-7.

[63] G. R. Joldes, A. Wittek, and K. Miller, “Real-time nonlinear finite element computations on GPU – Application to neurosurgical simulation,” *Computer Methods in Applied Mechanics and Engineering*, vol. 199, no. 49–52, pp. 3305–3314, Dec. 2010, doi: 10.1016/J.CMA.2010.06.037.